4

Gas Giants

AGUSTÍN SÁNCHEZ-LAVEGA, LAWRENCE A. SROMOVSKY, ADAM P. SHOWMAN, ANTHONY D. DEL GENIO, ROLAND M. B. YOUNG, RICARDO HUESO, ENRIQUE GARCÍA-MELENDO, YOHAI KASPI, GLENN S. ORTON, NAIARA BARRADO-IZAGIRRE, DAVID S. CHOI AND JOHN M. BARBARA

4.1 INTRODUCTION

The gas giants (Jupiter and Saturn) and icy giants (Uranus and Neptune) are fluid planets with atmospheres primarily made of hydrogen and helium. The part of their atmospheres accessible to remote sensing occupies only a small fraction of their radii (0.05%). Clouds and hazes form around the 1 bar altitude pressure level and extend vertically, according to the thermochemical models, in a layer with a thickness of ~200–500 km where temperature increases with depth (usually known as the "weather layer"). Clouds made of NH_3, NH_4SH, H_2O (in Jupiter and Saturn), with the addition of CH_4 (in Uranus and Neptune), cover the planet in stratified layers that are mixed with unknown chromophore agents. Dynamical phenomena in the weather layer shape different cloud patterns that define the visible appearance of these planets. In the thermal part of the spectrum clouds act as opacity sources providing brightness contrasts. The ensemble of cloud morphologies in terms of shapes, sizes and albedos allows their use as tracers of the atmospheric motions in the weather layer (Fig. 4.1). This is the main tool employed so far to study the winds on these four planets. Tables 4.1 and 4.2 present their relevant orbital and physical properties.

The atmospheres of these planets extend to a substantial part of their volume. Hydrogen is mostly in its molecular form (H_2), but at high pressures inside the planet (pressures above ~1.4–3 Mbar) the separation between H_2 molecules is of the order of their size, and hydrogen becomes an electrical conductor (a fluid metal). At $p \geq 3$ Mbar, dissociation of the molecule leads to an atomic metallic state (liquid). At much higher pressures theoretical calculations predict that hydrogen becomes a degenerate plasma. At the centre of these planets a rocky core is expected to exist according to some formation scenarios (Pollack et al., 1996; Guillot, 2005). Both theory and measurements of their gravitational fields indicate the presence of cores of 5–10 Earth mass for Jupiter and 10–20 Earth mass for Saturn. According to current models (see Guillot, 1999), the neutral atmosphere of Jupiter (a hydrogen and helium mixture) extends down to about ~15 000 km in Jupiter (0.2 of its radius) and in Saturn down to ~30 000 km (0.5 of its radius). Uranus and Neptune are less massive than the two gas giants, and models of their interiors indicate that, below the molecular atmosphere of hydrogen and helium, at pressures around 0.1 Mbar ($T \sim 2000$ K), a transition occurs where a mixture of ices (water, ammonia and methane) in ionic state is predicted, perhaps mixed with some heavier material. Accordingly, the neutral atmospheres of Uranus and Neptune extend down to about ~5500 km to ~3500 km (0.2–0.15 of their radius).

Table 4.1. *Orbital data*

Planet	Mean distance to Sun ($\times 10^8$ km)	Orbital eccentricity	Orbital tilt (deg)	Orbital period (yr)
Jupiter	7.78	0.0483	3.08	11.86
Saturn	14.27	0.0560	26.7	29.46
Uranus	28.69	0.0461	97.9	84.01
Neptune	44.96	0.0097	28.8	164.79

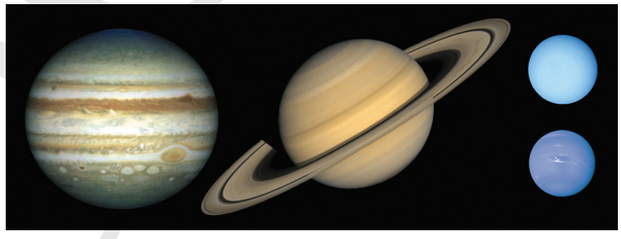

Figure 4.1 Visual appearance of Jupiter, Saturn, Uranus and Neptune, to scale. Credit: NASA/JPL.

The giant fluid planets have oblate spheroid shapes (Table 4.3) without rigid observable surfaces. Because of this geometry two definitions of latitude are used: planetographic latitude (φ_g), defined by the angle from the perpendicular to the tangent to the surface intersecting the semi-major axis of the ellipse, and planetocentric latitude (φ_c), relative to the centre of the ellipse (Sánchez-Lavega, 2011). The two are related by the formula

$$\tan \varphi_g = \left(\frac{R_e}{R_p}\right)^2 \tan \varphi_c, \tag{4.1}$$

where R_e and R_p are the equatorial and polar radius, respectively. The vector radius that gives the distance of a point at the surface spheroid to the center of the planet can be expressed as a function of R_e and R_p as

$$R(\varphi_c) = \frac{R_e R_p}{\sqrt{R_e^2 \sin^2 \varphi_c + R_p^2 \cos^2 \varphi_c}}. \tag{4.2}$$

Table 4.3 gives the relevant energy parameters for the four planets, being the effective and equilibrium temperatures T_{eff} and T_{eq} (for definitions, see Sánchez-Lavega, 2011).

Table 4.2. *Main physical properties*

Object	R_{mean}	M_p (kg)	Density (g cm^{-3})	g (m s^{-2})	Rotation period (hr)	Oblateness
Jupiter	71 300	1.90×10^{27}	1.33	22.88	9.84	0.061
Saturn	60 100	5.68×10^{26}	0.69	0.950	10.65[a]	0.09
Uranus	25 500	8.68×10^{25}	1.32	0.869	17.24	0.03
Neptune	24 800	1.02×10^{26}	1.64	11.00	16.11	0.03

[a] Not well constrained, value in the range 10.58–10.83 hr.

Table 4.3. *Energy in the outer planets*

Object	Geometric albedo	Insolation (W m^{-2})	Internal (W m^{-2})	T_{eff} (K)	T_{eq} (K)
Jupiter	0.52	50.6	5.44	124.4	113
Saturn	0.47	15.1	2.01	95	83
Uranus	0.51	3.72	0.042	59.1	60
Neptune	0.41	1.52	0.433	59.3	48

4.2 VERTICAL ATMOSPHERIC STRUCTURE

The temperature structure of gas giant atmospheres in the outer Solar System has been explored by several different approaches:

- The Galileo mission sent a probe into Jupiter's atmosphere in 1995 that made direct measurements in a single location.
- Measurements of the phase delay of radio signals from spacecraft occulted by planetary atmospheres have been inverted to produce a profile of refractivity as a function of altitude, which is converted into density and then temperature assuming knowledge of the mean-molecular weight as a function of altitude and the ideal gas law.
- Measurements of the attenuation of starlight or sunlight by atmospheric molecules have been similarly inverted to determine temperature profiles, assuming no attenuation by particulates.
- Most generally, the measurement of thermal emission by atmospheric constituents that are uniformly mixed has been inverted to derive temperature structures and their variation as a function of position and time.

All of these approaches have been used by spacecraft, which include the Pioneer 10 and 11 missions to Jupiter and Saturn, the Voyager 1 and 2 missions to all the outer planets, the Galileo orbiter and probe mission, and the Cassini mission Jupiter flyby and its long-term operations in orbit around Saturn. Earth-proximal spacecraft, such as the Spitzer Space Telescope and Herschel Space Telescope, have also made sensitive measurements of disk-averaged thermal emission spectra that have been inverted to determine or constrain temperatures. Spatially resolved measurements of thermal emission have also been made from ground-based observatories that track not only the variability of temperatures spatially, but their variability in time.

Similar to the Earth's atmosphere, the structure of the atmospheres of the outer planets can be divided into distinct regions, including the troposphere, where energy transport by winds dominates over radiative transport, and the stratosphere, where radiative transport dominates over convective transport. Above the stratosphere is the thermosphere, a region where conduction becomes the dominant means of energy transport and molecular diffusion takes place. Above the thermosphere is the ionosphere, a region that includes charged particles among the neutral atmosphere. Below, we discuss our knowledge of temperature structures "from the bottom up."

Unlike the Earth's troposphere, where meridional transport prevents the atmosphere from becoming fully adiabatic, the lapse rates of outer-planet tropospheres appears to be fully consistent with adiabatic conditions. Because of their rapid rotation rates and large radii, Coriolis forces dominate convection, and meridional flow is much slower than zonal flow. In addition, each of the outer planets except for Uranus emits more total energy than it receives from the Sun and thus energy is dominated by thermal upwelling from below. Thus, in the absence of condensation and latent heat effects, and assuming the perfect gas law, the lapse rate is

$$\frac{dT}{dz} = \frac{-mg}{C_p}, \tag{4.3}$$

where m is the mean molecular weight, g the local gravitational acceleration, and C_p is the molar heat capacity at constant pressure. The primary constituent of these atmospheres is molecular hydrogen, and its heat capacity is a function of temperature both because of its rotational degrees of freedom and because it is a homonuclear molecule with two states with proton spins parallel (ortho-H_2) and antiparallel (para-H_2). Helium is the second most abundant molecule and, as a monatomic molecule, has only translational degrees of freedom and a fixed molar specific heat. For the deeper atmospheres of Jupiter and Saturn, where water vapor condenses, and for Uranus and Neptune, whose atmospheres are cold enough for methane to condense, there are significant changes to the lapse rate arising from latent heat release. Ammonia also condenses in these atmospheres, but its latent heat effects are relatively small because of its small mixing ratio and small latent heat. The Galileo probe entered an anomalously dry and cloudless region of the atmosphere and temperatures measured during its descent through the troposphere clearly traced the expected dry adiabat (Seiff et al., 1998). Magalhães et al. (2002) used the Galileo probe temperature measurements to derive a static stability that varies between 0.0 and 0.2 K km^{-1} in the 1–22 bar region, with a measurement uncertainty of ~0.1 K km^{-1}, although these values may be unique to the anomalously dry region into which the probe descended.

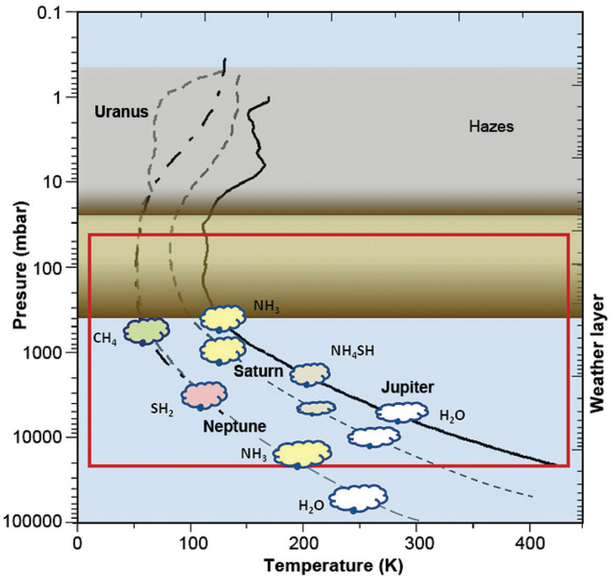

Figure 4.2 Temperature structures and cloud layers of the outer planets. The weather layer, where wind data are available, is highlighted by the red rectangle.

For the outer planets, the demarcation between the troposphere and stratosphere is particularly easy to delineate (Fig. 4.2). The stratospheres of all the outer planets have an "inverted" structure, with temperature rising with altitude. Thus, the temperature minimum of each planet (around 100 mbar) is usually described as the tropopause, although it may be as much as a scale height higher than the location where the lapse rate becomes smaller than the adiabatic one (around 400 mbar pressure). The rise in temperatures is caused by radiative equilibrium with absorbed sunlight: ultraviolet radiation absorbed by gaseous photodissociation reactions, visible radiation by stratospheric aerosols, and near-infrared radiation by methane gas absorption bands. This heating is balanced by radiative cooling in the mid-infrared by hydrocarbons, chiefly acetylene and ethane, byproducts of photodissociation of methane, as well as methane itself. The stratospheric temperature profiles of the outer planets generally correspond to the absorption characteristics expected of these sources of solar energy deposition, to the extent that they can be measured independently. The rise of temperatures at even lower pressures in the thermosphere is documented by ultraviolet occultation measurements and is not well understood, but is expected to be at least partially the result of deposition of energy by breaking of upwelling waves.

4.3 PLANETARY ROTATION AND REFERENCE FRAMES

It has been established since early in the twentieth century that the motions of cloud features in the Jupiter and Saturn atmospheres are east–West (zonal), and that their rotation periods in the space frame (the time needed to make a full rotation around the planet) are shorter at the equatorial latitudes than for the rest of the planet. This was called "differential rotation" for these

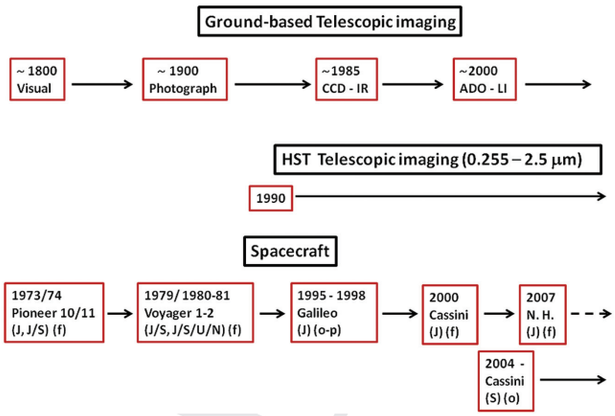

Figure 4.3 Giant planet imaging methods in time. Acronyms: J, S, U, N – giant planet initials; CCD – charge-coupled detectors (digital); ADO – adaptive optics; LI – lucky imaging; HST – Hubble Space Telescope; N. H. – New Horizons; f, o, p – spacecraft trajectories (flyby, orbit, probe).

two planets and was the first constraint on the planet rotation, although representing atmospheric motions. However, to transform these rotation periods to wind velocities it is necessary to introduce a reference frame linked to the true planet rotation.

The rotation rates of Jupiter, Saturn, Uranus and Neptune are taken to be those of their magnetic fields, which are assumed to be tied to the deep planetary interiors and represent the bulk rotation of the planet (Table 4.2). The rotation of the magnetic field can be measured indirectly by means of the modulated radio emission produced by accelerated charged particles trapped in the field lines. This rotation system is known as System III in the four gaseous planets. In the case of Saturn, the rotation axis and magnetic field are closely aligned, making it difficult to establish the radio rotation period. In addition, it has been found that Saturn's rotation System III, based on the radio rotation period, varies with time (on the order of 15 minutes) and splits into different values in the northern and southern hemispheres, apparently due to complex interactions in its ionosphere and magnetosphere that are not fully understood (Sánchez-Lavega, 2005; Gurnett et al., 2010). Theoretical estimates using the shape of the planet (Anderson and Schubert, 2007), potential vorticity (Read et al., 2009) and gravitational moments (Helled et al., 2015) produce rotation periods that are 5–7 minutes faster than the Voyager measurement. Until a definitive rotation rate is obtained, the recommended value for Saturn's rotation rate is that measured during the Voyager flybys in 1980 and 1981 to make previous atmospheric dynamic studies coherent. The zero longitude for System III on each planet is also arbitrary, but is defined by the International Astronomical Union (Archinal et al., 2011).

4.4 JUPITER AND SATURN WIND DATA

4.4.1 Available Datasets

Winds in the fluid planets are essentially inferred in three ways: (a) above the clouds, from temperature measurements and the use of the thermal wind equation; (b) at cloud level, from track-

Table 4.4. *Summary of zonal wind meridional profiles measured for Jupiter at visible wavelengths*

Year	Spacecraft / telescope	Max. resolution (km per pixel)	Reference
1979	Voyager 1 and 2 (ISS[a])	100	Ingersoll et al. (1981); Limaye (1986); Maxworthy (1984)
1995	Galileo probe		Atkinson et al. (1998)
	Galileo orbiter		Vasavada et al. (1998)
1995–98	HST (WFPC2[b])	140	García-Melendo and Sánchez-Lavega (2001)
2000	Cassini	120	Porco et al. (2003); García-Melendo et al. (2011a); Asay-Davis et al. (2011); Galperin et al. (2014b)
2008	HST (WFPC2[b])	160	Simon-Miller and Gierasch (2010); Asay-Davis et al. (2011)
2011	High-res amateur data	380	Barrado-Izagirre et al. (2013)
2015	HST (WFC3)	130	Simon et al. (2015)
2016	High-res amateur and HST (WFC3)	380, 130	Hueso et al. (2017a)
2009–16	HST (WFC3)	130	Tollefson et al. (2017)

[a] ISS: Imaging Science Subsystem.
[b] WFPC2: Wide Field and Planetary Camera 2.

Table 4.5. *Summary of zonal wind meridional profiles measured for Saturn at visible wavelengths*

Year	Spacecraft / telescope	Max. resolution (km per pixel)	Reference
1980–1981	Voyager 1 and 2 (ISS[a])	50–150	Smith et al. (1981, 1982); Ingersoll et al. (1984); Sánchez-Lavega et al. (2000)
1996–2004	HST (WFPC2[b])	260	Sánchez-Lavega et al. (2003, 2004)
2004–2009	Cassini	30–160	Porco et al. (2005); Vasavada et al. (2006); Del Genio et al. (2007); Del Genio and Barbara (2012); García-Melendo et al. (2010, 2011b); Sánchez-Lavega et al. (2007)

[a] ISS: Imaging Science Subsystem.
[b] WFPC2: Wide Field and Planetary Camera 2.

ing the motions of individual features; (c) below the clouds, and until now constrained indirectly from modeling, with the sole exception of in situ measurements by the Galileo entry probe.

Zonal wind measurements from cloud tracking of Jupiter began in the twentieth century and were based on the long-term tracking of long-lived well-contrasted features. Wind measurements of Saturn were restricted to the occurrence of large-scale storms only at a few latitudes. Therefore, the details of the wind systems of both planets remained poorly known until Voyagers 1 and 2 flew past Jupiter in 1979 and Saturn in 1980–81. Accurate and tabulated zonal winds for Jupiter and Saturn have been published by Limaye (1986) and Sánchez-Lavega et al. (2000) respectively. The Galileo Probe entered Jupiter's atmosphere in 1995, allowing in situ measurements of velocities at a single equatorial location (Atkinson et al., 1998). Observations from the Galileo orbiter led to precise measurements of Jovian winds over some localized areas near the equator and large vortices like the Great Red Spot (Vasavada et al., 1998). The Cassini spacecraft obtained further high-resolution observations of Jupiter in 2000 (Porco et al., 2003) – see below. The New Horizons mission to Pluto flew by Jupiter in 2007, providing high-resolution wind data for particular latitudes (Reuter et al., 2007). Cassini has been successfully observing Saturn for several years, obtaining several full zonal wind profiles at different cloud altitudes (Porco et al., 2005; Vasavada et al., 2006; Choi et al., 2009; García-Melendo et al., 2011b).

Figure 4.3 and Tables 4.4 and 4.5 summarize the available sources used to obtain wind data for the giant planets. Intermediate periods of time between the different space missions have been partially covered by observations obtained from the Hubble Space Telescope (HST). The first Jupiter image set from HST was obtained in 1991, and zonal wind profiles have been obtained over several years as summarized in Table 4.4. Hubble also observed Saturn before Cassini arrived at the planet, and the HST results are summarized by Sánchez-Lavega et al. (2003, 2004).

Additionally, high-resolution ground-based observations of the giant planets have become possible in recent times with the advent of fast CCD and CMOS cameras that allow filming of the planet to obtain a stream of frames that can be selected in terms of their quality and coregistered into a high signal-to-noise ratio image that can reveal small-scale cloud features. This "lucky imaging" technique (Law et al., 2006) is currently used by a broad community of amateur observers resulting in frequent observations of Jupiter and Saturn with successful retrievals of full zonal wind profiles for Jupiter (Barrado-Izagirre et al., 2013) and detailed studies of storms and large-scale disturbances (Sánchez-Lavega et al., 2012).

Voyager Data

The NASA Voyager 1 and 2 spacecraft performed the "Grand Tour" of the outer solar system. Voyager 1's trajectory was planned for encounters with Jupiter (March 5, 1979) and Saturn (November 12, 1980), and Voyager 2 performed flybys of Jupiter (July 9, 1979), Saturn (August 25, 1981), Uranus (January 24, 1986) and Neptune (August 25, 1989). Data were gathered over about three months centered on the encounter date. Wind studies were essentially done with two instruments.

Imaging Science System (ISS) This consisted of narrow-angle (focal length = 1502.4 mm, f/8.5, instrument FOV = 0.424°) and wide-angle (focal length = 200.5 mm, f/3.5, instrument FOV = 3.169°) vidicon cameras with a photoconductive Se–S detector. Because of the optical distortion, a grid-dot pattern was used with appropriate software for navigation (camera pointing). The narrow-angle camera was equipped with a set of six broadband filters covering the spectral range 0.28–0.64 μm, and the wide-angle camera incorporated seven filters covering the spectral range 0.35–0.64 μm but incorporating a narrow sodium line filter and a methane absorption band filter at 619 nm. Details of the instrument can be found in Smith et al. (1977).

Infrared Spectroscopy and Radiometry Investigation (IRIS) This consisted of two Michelson interferometers covering the spectral ranges 17–170 μm and 1.4–10 μm, and a radiometer covering the range 0.4–1.2 μm. They shared a 50 cm Cassegrain telescope with a circular field of view of 0.25° (Hanel et al., 1977). Because of a small misalignment during the cruise phase, the IRIS on Voyagers 1 and 2 operated only in the spectral range 4–55 μm, with a lower responsivity at some wavelengths in the Voyager 2 case. This instrument provided infrared spectra that allowed, among others, temperature measurements used to retrieve thermal winds (see Section 4.7.3).

Cassini Data

The NASA/ESA spacecraft Cassini–Huygens flew past Jupiter on a near-equatorial trajectory in late 2000 / early 2001, with the closest approach to the planet around 136 Jupiter radii on December 30 (Porco et al., 2003). Between October 1, 2000 and March 22, 2001 it obtained sevaral long sequences of observations of the planet. During Cassini's approach to Jupiter, most of the hemisphere visible to the spacecraft was illuminated by the Sun. This provided an excellent opportunity to monitor the evolution of the whole atmosphere at visible wavelengths over a two-month period up to the closest approach, which was done using the narrow-angle camera. Such continuous global observations could not be taken by the Galileo spacecraft and will not be possible with the forthcoming Juno spacecraft either. Cassini went into Saturn orbit on June 30, 2004. The Saturn approach period from February to June 2004 and the first orbit from June to October 2004 provided relatively low-resolution multi-spectral images at moderate phase angles. The best imaging sequences for winds were from 2005 and 2007, when low to moderate phase-angle orbits provided high-resolution hemispheric or near-global coverage. Brief moderate-resolution image sequences have been obtained in most other years. The Cassini Saturn Orbiter includes three instruments that provide information on Saturn zonal winds.

Imaging Science Subsystem The ISS (Porco et al., 2004) is a near-ultraviolet, visible and near-infrared imaging system with wide- and narrow-angle cameras covering a range of wavelengths from 200–1100 nm. The narrow-angle camera has a 0.35° field of view (~6 μrad/pixel), and the wide-angle camera has a 3.5° field of view (~60 μrad/pixel) with its lower wavelength limit at 380 nm. The filters (see Table 8 in Porco et al., 2004) include wide-bandpass filters over the whole range of frequencies, and narrow-bandpass filters at specific wavelengths of interest such as methane bands at 619, 728, and 889 nm, and H-α/lightning at 656 nm. Visible images correspond primarily to reflected light from Jupiter's and Saturn's cloud tops and methane band filters are sensitive to hazes in the upper troposphere and lower stratosphere. The clouds and hazes can be tracked between images using manual feature tracking, line displacement correlation tracking or automated feature tracking methods to retrieve estimates of wind speeds at each altitude. For Jupiter, a subset of the Jupiter ISS images taken near closest approach have been preprocessed, mapped onto a longitude–latitude grid and made generally available for analysis via the NASA Planetary Data System (Vasavada et al., 2008). This dataset spans almost four Jupiter rotation periods in mid-December 2000 covering the time when the Sun–Jupiter–Cassini angle was close to zero. These images were taken in the 455 nm blue BL1, 750 nm continuum CB2, and 727 nm and 889 nm methane MT2 and MT3 filters, every 63 min as the planet rotated below the spacecraft. Several authors have used this dataset to track clouds and study various features of Jupiter's atmosphere and zonal jets (Salyk et al., 2006; Choi and Showman, 2011; Galperin et al., 2014b), as will be discussed in detail later. An example of this kind of analysis is shown in Fig. 4.4 from Galperin et al. (2014b).

Several studies of Saturn jets based on Cassini ISS images are also available (Porco et al., 2005; Vasavada et al., 2006; Del Genio et al., 2007; Sánchez-Lavega et al., 2007; García-Melendo et al., 2009, 2010, 2011b; Del Genio and Barbara, 2012), with data obtained on different dates for different latitudes, and with relevant results for the vertical structure of the jets and assessments of their temporal stability and possi-

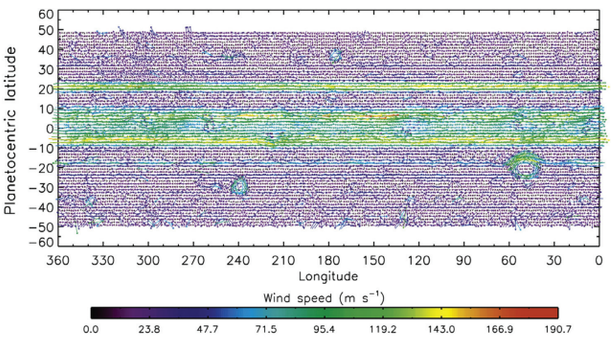

Figure 4.4 Jupiter's cloud-level velocity field as observed by Cassini on December 11–12, 2000. From Galperin et al. (2014b). The vectors are plotted 1.5° apart, and they are subsampled by a factor of three from the full velocity field.

ble variability at equatorial latitudes (Li et al., 2011; Sánchez-Lavega et al., 2016). Complete tabulated wind profiles in the cloud deck and upper hazes based on five years of Cassini ISS data are given by García-Melendo et al. (2011b).

Visual and Infrared Mapping Spectrometer The VIMS (Brown et al., 2004) is also used for feature tracking but at the deeper ammonium hydrosulfide cloud level in 5 μm images (Baines et al., 2005; Choi et al., 2009). Unlike ISS, which can image for multiple Saturn rotations near apoapsis, VIMS can only produce images suitable for tracking during brief periods not far from periapsis. Near-global VIMS mapping of Saturn was performed in 2006, with specific latitude bands sampled in feature tracks at other times during the mission.

Composite Infrared Spectrometer The CIRS (Flasar et al., 2004b) derives latitudinal temperature gradients in the upper troposphere and stratosphere from thermal infrared spectral radiances (Flasar et al., 2004a, 2005; Fletcher et al., 2007, 2010; Li et al., 2013), from which mean zonal winds can be derived using the thermal wind equation. CIRS is a Fourier transform spectrometer sensitive to wavenumbers 10–1400 cm^{-1} (7 μm to 1 mm wavelengths) with a spectral resolution of 0.5–15.5 cm^{-1}. The far-infrared range (10–600 cm^{-1}) is covered by a polarization interferometer, and the mid-infrared range (600–1400 cm^{-1}) by a Michelson interferometer. In both cases the field of view is much smaller than the ISS. CIRS has two far-infrared detectors with a 3.9 mrad field of view and ten mid-infrared detectors with a 0.273 mrad field of view. The instrument can take data in both nadir and limb viewing modes. CIRS data can be used in two main ways relevant to zonal jets. Three-dimensional temperature fields can be combined with wind data and the thermal wind equation to derive winds at levels where none can be retrieved directly (see Sections 4.7.2 and 4.7.3; e.g., Flasar et al., 2004b). The temperature fields obtained from CIRS data can also be used – in principle – to calculate heat transport diagnostics such as $u'T'$ and $v'T'$. These diagnostics are used to determine the potential energy transfer terms in the Lorenz atmospheric energy cycle (Lorenz, 1955), which can be used to determine how important different instabilities are in driving the zonal jets.

4.5 JUPITER AND SATURN: METEOROLOGICAL FEATURES

The visible appearance of both Jupiter and Saturn is dominated by the presence of zonal (east–west) bands of alternating albedo, axisymmetric with the rotation axis. This pattern is formed by "white" (high-albedo) bands called "zones" and "reddish" (lower-albedo) bands known as "belts" that remain at approximately fixed latitudes year to year (Fig. 4.5). A similar pattern is replicated at lower levels, as observed in thermal-infrared images (Fig. 4.6). Immersed within the bands is a plethora of cloud structures, some coherent, some turbulent or chaotic, from small and short-evolution timescales to large and long-evolution timescales (Fig. 4.7). Discrete meteorological features can be classified accordingly in the following basic types (Fig. 4.8).

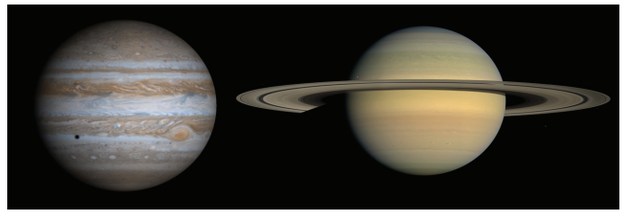

Figure 4.5 Jupiter's and Saturn's bands. Both images were acquired by the Cassini ISS camera and represent nearly true-color images of the planets. Both planets are represented to scale. Credit: NASA/JPL.

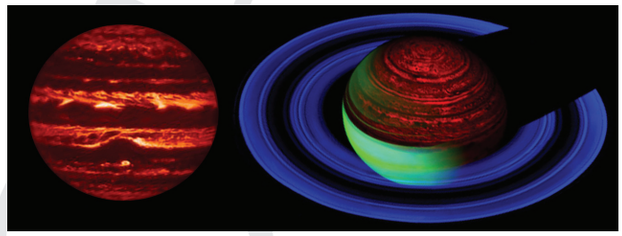

Figure 4.6 Jupiter and Saturn in infrared wavelengths. Bright areas show regions of lower cloud content where the inner heat can escape more easily. Jupiter's image was acquired at a wavelength of 5.0 μm with the NASA IRTF. Saturn's image was acquired by the VIMS instrument on board Cassini. Red is for thermal IR radiation from the night-side of the planet. Green and blue correspond to solar radiation in near-infrared wavelengths reflected from the southern hemisphere of the planet and its rings. Credit: NASA/JPL.

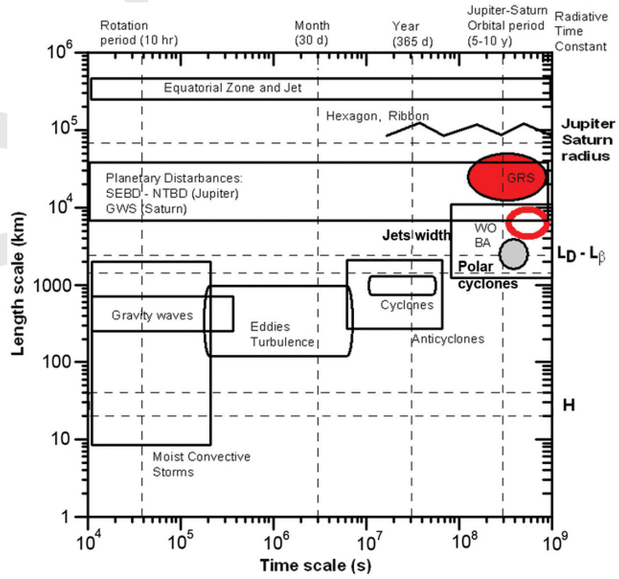

Figure 4.7 Horizontal and temporal dynamical scales observed on Jupiter and Saturn. The relevant length scales are the planetary radius (R_p), Rossby deformation radius (L_D), Rhines scale (L_β) and vertical scale height (H). See Sánchez-Lavega (2011) for definitions.

Coherent Vortices Large-scale and long-lived stable oval spots, most of them with anticyclonic vorticity, such as the Great Red Spot or the White Ovals (later BA) on Jupiter, or the Brown Spots (BS) and North Polar Spot (NPS) on Saturn.

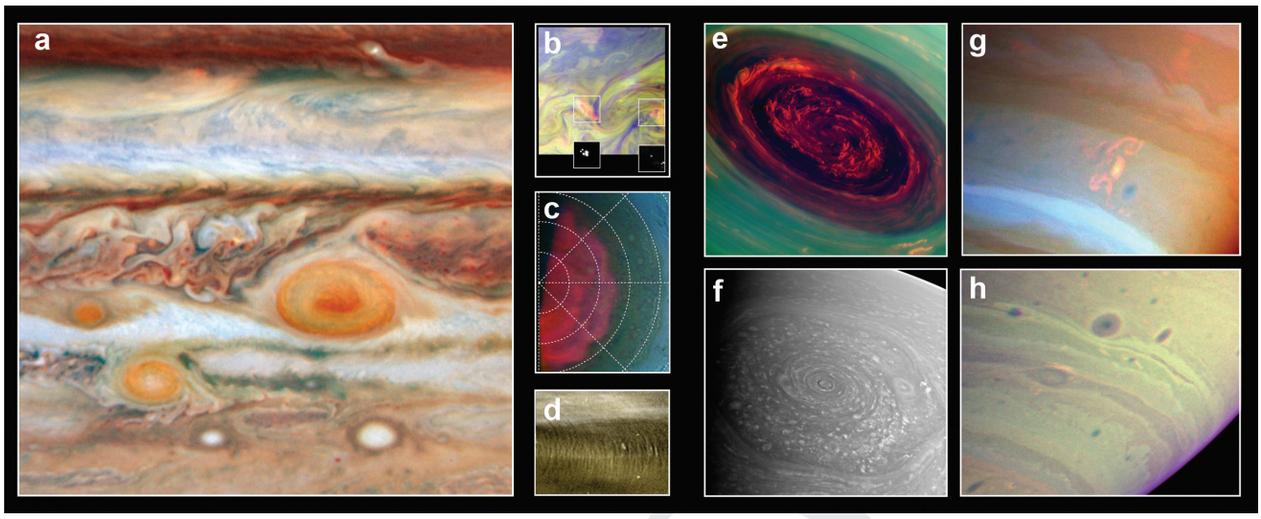

Figure 4.8 Meteorological features on Jupiter (a–d) and Saturn (e–h). (a) Jupiter's Great Red Spot, Oval BA and several other ovals, storms and equatorial dark projections from HST observations (de Pater et al., 2010). (b) Lightning storms observed by Galileo (Gierasch et al., 2000). (c) Polar projection of HST images showing a system of circumpolar waves marked in the hazes (Barrado-Izagirre et al., 2008). (d) New Horizons images of gravity waves in the equatorial region of the planet (Reuter et al., 2007). (e) Cyclonic vortex at Saturn's north pole imaged by Cassini ISS (PIA 14944). (f) Saturn's polar hexagonal wave feature and polar clouds. (g) Typical convective storm in the southern-hemisphere "storm alley" (Dyudina et al., 2007). (h) Normal vortices on Saturn's south hemisphere. All images are false color. Credit: NASA/JPL/ESA.

Coherent cyclones are in general more elongated with shorter lifetimes, such as the so-called "barges" on Jupiter.

Convective Storms Rapidly evolving spots that change their brightness and size (from small to large features) in a matter of few days, indicative of strong moist convective storms with associated lightning that can be observed on the night-side of the planet for Jupiter (Little et al., 1999; Gierasch et al., 2000) and Saturn (Dyudina et al., 2010), and in extreme cases also in the day-side (Dyudina et al., 2013). On Jupiter, the storms and adjacent areas constitute the only locations where clear spectroscopic signatures of water (Simon-Miller et al., 2000) or ammonia ices have been found (Baines et al., 2002; Reuter et al., 2007). On Saturn, the large Great White Spot of 2010 and 2011 (Sánchez-Lavega et al., 2011; Sayanagi et al., 2013) provided a clear indication of ammonia and water ice particles (Sromovsky et al., 2013). Models of moist convection for the strongest storms on both planets (Hueso and Sánchez-Lavega, 2001, 2004) require water condensation instead of ammonia condensation as the energy source for the storms in order to explain their cloud-top altitude and observed phenomonology.

Planetary-Scale Disturbances These are the most impressive features on Jupiter and Saturn since they can change the entire aspect of a zone or belt. The atmospheres of both planets develop atmospheric perturbations that can grow into planetary-scale disturbances that grow to cover a full latitudinal band of the planet. Jupiter presents such disturbances in its North Temperate Belt (Sánchez-Lavega et al., 2008a, 2017) and South Temperate Belt (Sánchez-Lavega et al., 1996); see Fig. 4.9. Both start with one or several convective features that produce fresh white clouds that are sheared by the zonal winds (Fletcher et al., 2017). Saturn's atmosphere develops larger disturbances about once every 30 years in eruptions called "Great White Spots" (GWS) or Great Storms (Sánchez-Lavega, 1994). The 1990 GWS occurred at the equator of the planet and was observed with the HST (Barnet et al., 1992) and from ground-based telescopes (Sánchez-Lavega et al., 1991) showing the interaction of the bright storm nucleus with the ambient winds. The last GWS started in December 2010 at north mid-latitudes

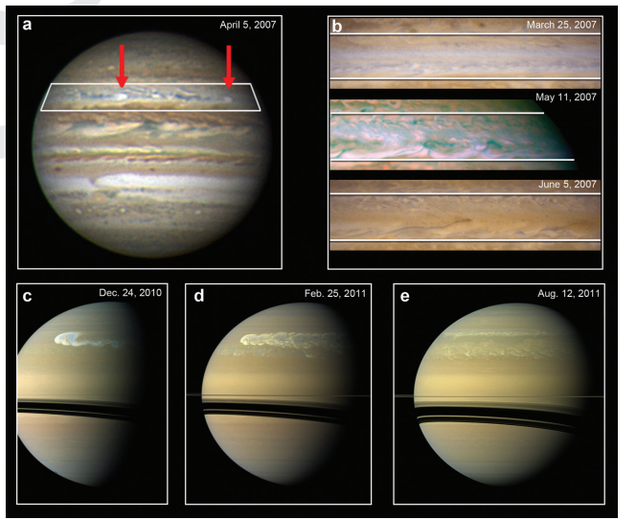

Figure 4.9 Large-scale disturbances on Jupiter and Saturn. (a) Double eruption in the North Temperate Belt in 2007 (Sánchez-Lavega et al., 2008a) with two convective features producing a turbulent wake in the fastest zonal jet on Jupiter. (b) Evolution of the North Temperate Belt from HST data, from the unperturbed state to highly turbulent structures characteristic of planetary-wide disturbance, to a quiet phase where the Belt has dissipated. (c) Set of Cassini ISS observations of Saturn's Great White Spot evolution (Sayanagi et al., 2013).

and its evolution was followed in detail from Cassini observations (Sayanagi et al., 2013) and high-temporal sampling from the ground (Sánchez-Lavega, 2011; Sánchez-Lavega et al., 2012). The disturbed atmospheres of Jupiter and Saturn take about a year to restore to their normal appearance, and the disturbances seem to modify only slightly the zonal jets at their latitudinal location.

Wave-Like Features At the equatorial boundary of the North Equatorial Belt of Jupiter there is a system of 10–12 large-scale dark projections (high emission at 5 μm, called "hot-spots") that have been interpreted as a large-scale trapped equatorial Rossby wave (Allison, 1990; Arregi et al., 2006; García-Melendo et al., 2011a). Other large-scale wave systems on Jupiter are observed in the South Equatorial Belt (Simon-Miller et al., 2012), in the North Equatorial Belt (at 15° N) (Li et al., 2006) and in the polar hazes in both hemispheres (Sanchez-Lavega et al., 1998a; Barrado-Izagirre et al., 2008). Short-scale waves have also been observed in the equatorial region of the planet since the Voyagers (Hunt and Muller, 1979) and have been interpreted as gravity waves (Flasar and Gierasch, 1986; Reuter et al., 2007; Arregi et al., 2009). Other similar wave systems observed at the equator during the New Horizons flyby (Reuter et al., 2007) have been interpreted as either gravity waves or Kelvin waves (Simon et al., 2015), or as equatorial Kelvin waves (Simon et al., 2015). Planetary waves on Saturn are long-lived and well localized in latitude, the most notorious being in the northern hemisphere: the "ribbon" (Smith et al., 1982; Sromovsky et al., 1983; Sánchez-Lavega, 2002; Sayanagi et al., 2010b) and the polar hexagon (Godfrey, 1990; Sánchez-Lavega et al., 2014).

Polar Cyclones At visible wavelengths and latitudes above 87°, both poles of Saturn show strong cyclonic vortices that enclose a region less cloudy than their surroundings (Sánchez-Lavega et al., 2006; Dyudina et al., 2008; Antuñano et al., 2015; Sayanagi et al., 2017); see Fig. 4.8.

4.6 WIND MEASUREMENTS FROM CLOUD MOTIONS

The wind field at cloud-top level for Jupiter and Saturn has been inferred by tracking the motions of cloud features in a time sequence of images. This assumes that the cloud features behave as passive tracers. Passive cloud tracers must preserve their integrity over the time interval used to measure their motion. Since the atmospheres of Jupiter and Saturn have zonal jets, large synoptic-scale vortices and large storms, the motions of features in different meteorological structures at the same latitude can be quite different. Large details such as synoptic-scale vortices, convective clouds or turbulent regions may introduce spurious components in velocity measurements of the zonal jets and must be avoided (García-Melendo and Sánchez-Lavega, 2001), but high-resolution images of those structures can resolve their internal motions (Choi et al., 2007; Hueso et al., 2009).

Zonal winds can be measured for individual cloud tracers at the same latitude by measuring their longitudinal position at two different times. These measurements assume a particular rotation frame for the planet, which is usually System III for Jupiter and Saturn, defined by their respective angular velocities ($\Omega_{\mathrm{III\,Jup}} = 870.5366420°\,\mathrm{day}^{-1}$ and $\Omega_{\mathrm{III\,Sat}} = 810.7939024°\,\mathrm{day}^{-1}$; Seidelmann et al., 2007). If the images have been adequately navigated to minimize position errors, the tracer is at a latitude φ_c, the initial and final longitude positions are λ_1 and λ_2 (in degrees), and the respective measurement times are t_1 and t_2, then the velocity with respect to the reference rotation frame is

$$u(\varphi_c) = \frac{2\pi R(\varphi_c)\cos(\varphi_c)}{360°}\frac{\lambda_2 - \lambda_1}{t_2 - t_1}. \tag{4.4}$$

Estimated errors in the measurement of $u(\varphi_c)$ are given by the quotient between longitude measurement errors and the time difference $t_2 - t_1$. Therefore, the larger the time base, the smaller the velocity error. However, small cloud features are usually deformed and destroyed by horizontal wind shear, interactions with other tracers, and other dynamical processes, and the time base usually cannot be arbitrarily extended for more than a single planetary rotation. Manual pointing of individual cloud tracers is also prone to subjective errors in identifying the position of a small feature, but these misidentifications are usually obvious once the wind vectors are examined in the context of nearby features. If the tracer is long-lived, a much better procedure to estimate zonal velocity is to obtain several longitude measurements to extend the time base as much as possible, and then estimate the quotient $(\lambda_2 - \lambda_1)/(t_2 - t_1)$ by linear regression, substantially reducing errors associated with the drift velocity. The bigger downside to manual measurements is the low density of measured vectors.

4.6.1 One-Dimensional Brightness Correlation

Automatic methods for extracting zonal velocities have been highly successful in the measurement of wind fields in the atmospheres of Jupiter and Saturn. For time intervals short enough, most of the cloud tracers at a given latitude will survive more or less intact but will be shifted in longitude according to the background zonal wind. Images can be cylindrically projected onto rectangular maps, usually correcting the atmospheric limb-darkening by using either a Lambert function, an empirical Minnaert correction (Minnaert, 1941) or a high-pass filter. The comparison can be performed using the cross-correlation function

$$R_{fg}(\varphi, \lambda_j) = \sum_{i=1}^{N} f_\varphi(\lambda_i) g_\varphi(\lambda_i - \lambda_j), \tag{4.5}$$

where $f_\varphi(\lambda_i)$ and $g_\varphi(\lambda_i)$ are the albedo functions at the discrete longitude values λ_i at the specific latitude φ.

The maximum of the cross-correlation function gives us the longitude shift due to zonal wind motion, and the zonal flow speed is measured from Eq. (4.4). This procedure produces an *average zonal mean velocity*, and the set of retrieved velocities at a given pressure level for a complete set of latitudes is usually called the *average zonal mean velocity profile*. Figure 4.10 sketches the procedure. Variations of this technique have been

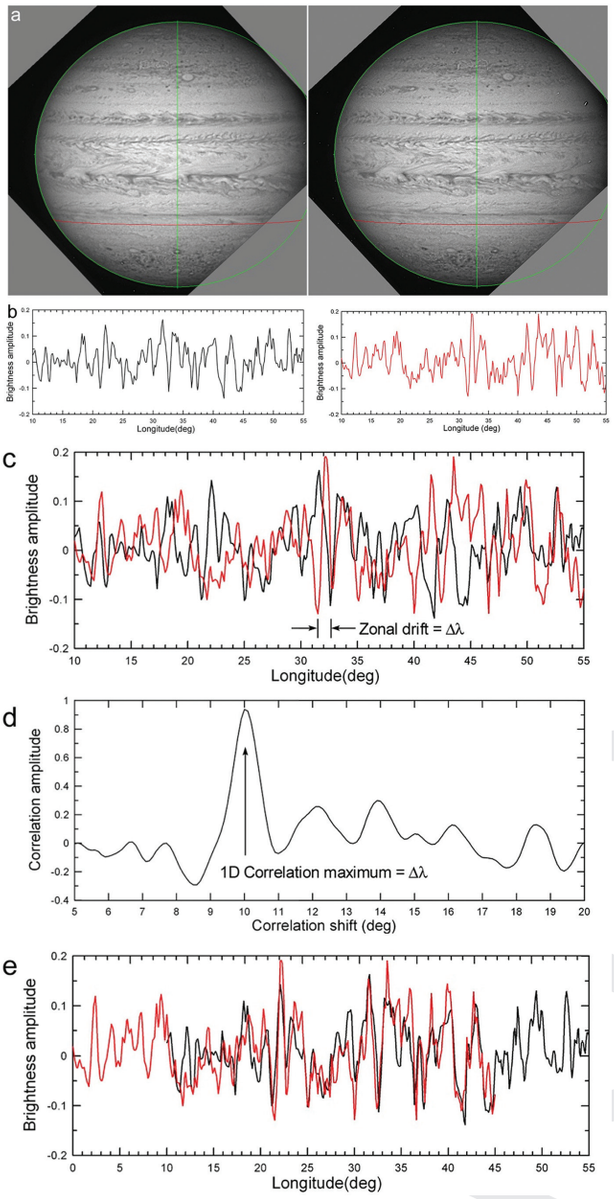

Figure 4.10 One-dimensional correlation illustration. (a) Navigated pair of Jupiter images taken by the HST on October 25, 1996, separated by one planetary rotation. The red parallel marks the position of the two longitude brightness scans to be compared by one-dimensional correlation. (b) Limb-darkening corrected and normalized longitude scans. (c) Both scans are shifted by a longitude increment $\Delta\lambda$ due to zonal wind motion. (d) Cross correlation function of scans depicted in panel (b) with a maximum for $\Delta\lambda$. (e) Brightness scans match after correcting zonal shift.

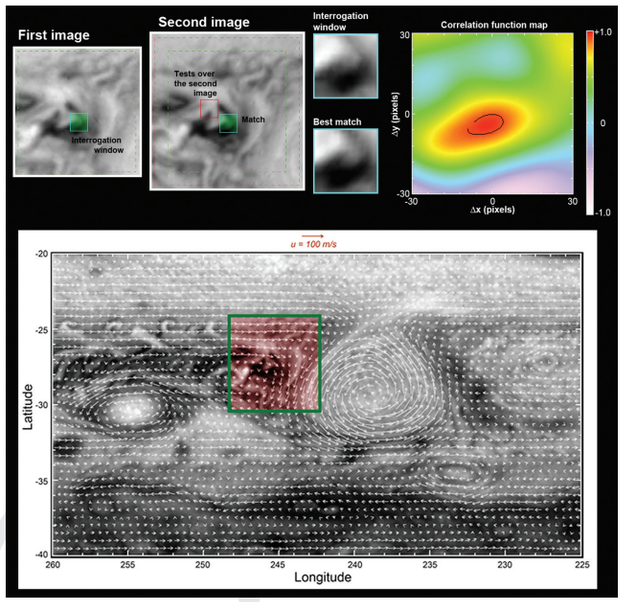

Figure 4.11 Two-dimensional image correlation. The first image is divided into small boxes f, with a size large enough to have distinguishable cloud features. A pixel box template g of the same size as in the first image is considered and moved in the second image, finding the correlation between f and g for each k, l displacement. The displacement that maximizes the correlation function is taken as a measure of the wind at the center of f.

used several times for Jupiter and Saturn (Limaye, 1986; Magalhaes et al., 1990; García-Melendo et al., 2011a; Barrado-Izagirre et al., 2013) with the main error sources associated to navigation uncertainties, intrinsic variability of the cloud tracers (Sánchez-Lavega et al., 2000), local dynamics such as waves, vortices or convection (García-Melendo and Sánchez-Lavega, 2001), and scarcity of tracers in some domains of the planet. Typical errors from space-borne observations at optical wavelengths are $\sim$10 m s^{-1}, but are higher when using infrared imaging instruments such as VIMS on Cassini (Choi et al., 2009).

4.6.2 Two-Dimensional Image Correlation

Image sets with enough spatial resolution (typically 100 km per pixel or better) can provide a two-dimensional field of winds over large regions of a planet (Salyk et al., 2006; Del Genio et al., 2007; Del Genio and Barbara, 2012; Galperin et al., 2014b) or for specific areas (Vasavada et al., 1998; Choi et al., 2007; Hueso et al., 2009; García-Melendo et al., 2013) by an implementation of two-dimensional image correlation algorithms. This technique works with cylindrical or polar projections of high-resolution images, which can be compared using a two-dimensional version of the cloud correlation algorithm. A sketch of how this procedure works appears in Fig. 4.11. The first image is divided into small subimages f with $N \times M$ pixels, ideally large enough to contain identifiable cloud features but small enough to obtain high-resolution results.

Only data provided by spacecraft observations of Jupiter and Saturn and by some HST observations of Jupiter with the Advanced Camera for Surveys (ACS) and WFPC2 and WFC3 instruments have the required spatial resolution. Typical results include measurements of well-defined cloud features with obvious outliers that are removed from the data using different criteria. Outliers can be produced by laminar elongated features or by the correlation coefficient of a pixel box match being too small. Two-dimensional cloud correlation algorithms generally differ more in their criteria for selecting and removing outliers than in the definition of the two-dimensional correlation func-

tion. Selection of elongated boxes in the first image renders a two-dimensional cloud correlation algorithm similar to the one-dimensional correlation algorithms discussed above.

Measurement errors scale roughly as the image resolution divided by the time interval used, and the main uncertainties come from small errors in image navigation and temporal evolution of the cloud features. Typical time separations are of the order of one planetary rotation (10 hr), allowing wind speeds to be resolved to a level of $1\,\mathrm{m\,s^{-1}}$. Images separated by 1–2 hr can also be used to retrieve the internal wind field of large vortices, and high-resolution images (15 km per pixel) with short time separations as small as 20 min have been used in a few cases (see, for instance, García-Melendo et al., 2013). In the latter cases error measurements of an individual tracer are of the order of $10\,\mathrm{m\,s^{-1}}$, but using a larger time separation between images is not generally possible since turbulent cloud features inside the large vortices of Jupiter rotate and distort severely in just one planetary rotation. The zonal average can be retrieved with higher precision from statistics of the individual features.

There are other alternatives to direct image correlation. Those tested in Jupiter are a streamline method applying one-dimensional correlation over streamlines (Sussman et al., 2010) and advection-corrected correlation image velocimetry (ACCIV), which has been tested successfully in Jupiter images separated by 10 hr (Asay-Davis et al., 2009). Larger time differences at high spatial resolution are not possible due to the strong distortion of cloud features in the turbulent atmospheres of Jupiter and Saturn in those timescales. The fluid dynamics literature is very rich in iterative image deformation methods used in image velocimetry applications; the interested reader is referred to Scarano (2002) and references therein. Globally, two-dimensional correlation methods give a greater number of wind vectors than cloud tracking, although results generally require very high-quality data and averages along a latitude band are usually necessary to measure the zonal winds with the highest possible precision.

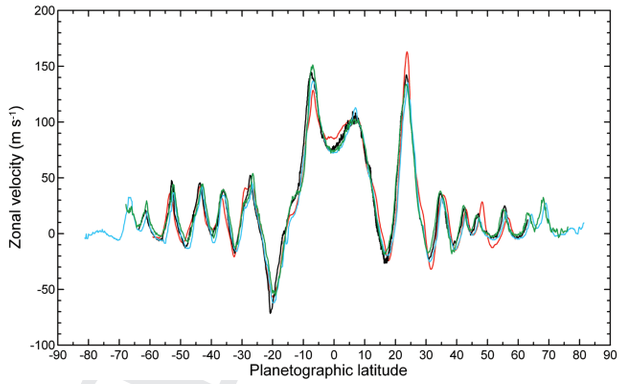

Figure 4.12 Jupiter zonal wind profiles. Red is from Voyager data (Limaye, 1986), black (García-Melendo et al., 2011a) and blue (Porco et al., 2003) are from Cassini data, and green is from HST data (García-Melendo and Sánchez-Lavega, 2001).

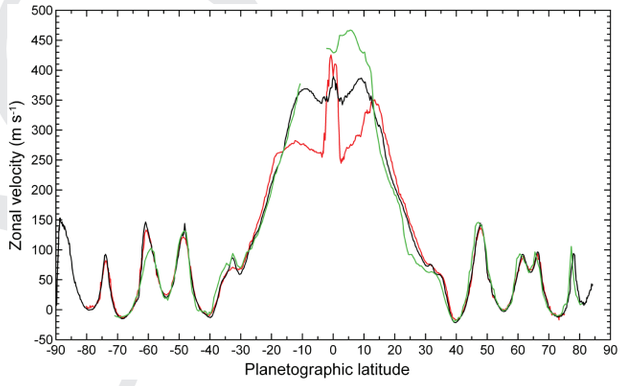

Figure 4.13 Saturn zonal wind profile. Green represents Voyager data (Sánchez-Lavega et al., 2000); black is Cassini imaging data in the continuum (350–500 mbar); red is Cassini imaging data in the strongly absorbing methane band at 890 nm (60–250 mbar) (García-Melendo et al., 2011b).

4.7 JUPITER AND SATURN: MEAN WIND AT CLOUD LEVEL

4.7.1 Upper Cloud Level

Jupiter has between seven and eight jets per hemisphere at the nominal ammonia cloud level (~700 mbar), as shown in Fig. 4.12. Its distribution is not symmetrical and is dominated by a strong equatorial jet with maximum velocities of $140\,\mathrm{m\,s^{-1}}$. A particular feature of Jupiter's zonal wind system is the presence of a strong eastward jet at 24° N with measured maximum velocities between $120\,\mathrm{m\,s^{-1}}$ and $180\,\mathrm{m\,s^{-1}}$ (Maxworthy, 1984; Limaye, 1986; Simon, 1999; García-Melendo and Sánchez-Lavega, 2001; Asay-Davis et al., 2011; Barrado-Izagirre et al., 2013; Sánchez-Lavega et al., 2017; Tollefson et al., 2017). There is no southern counterpart for the 24° N jet, only a $\sim 60\,\mathrm{m\,s^{-1}}$ jet at −27° S, very close to the location where the GRS sits (−23°). Perhaps the GRS presence accounts for the wind profile asymmetry at ~ ±24° latitudes, but the reason is unknown. Before the Cassini encounter with Jupiter in 2000, the equatorial jet always presented, from manual and automatic wind speed retrievals, an asymmetric double-peaked structure with maximum velocities of $140\,\mathrm{m\,s^{-1}}$ at −7° S, and $100\,\mathrm{m\,s^{-1}}$ at 7° N. Detailed analysis of spacecraft and ground-based images after the year 2000 showed that Jupiter's equatorial jet is actually symmetric with maximum velocities of $140\,\mathrm{m\,s^{-1}}$, but that the apparent asymmetry of the equatorial jet is due to the superposition of the westward phase velocity of a trapped Rossby wave (Asay-Davis et al., 2011; García-Melendo et al., 2011a; Barrado-Izagirre et al., 2013).

The first detailed zonal profiles for Saturn were retrieved from Voyager data at optical wavelengths (Ingersoll et al., 1984; Sánchez-Lavega et al., 2000). The use of broadband color filters did not allow an accurate determination of the pressure level that corresponded to the wind retrievals, but probably they were close to the 500–700 mbar level (probably the upper top of the ammonia cloud; Pérez-Hoyos and Sánchez-Lavega, 2006a). HST observations produced partial data that was difficult to interpret due to the presence of strong convective activity at the north equatorial region (Sánchez-Lavega et al., 2003). Cassini orbital insertion around Saturn in 2004 allowed the retrieval of detailed measurements of Saturn's wind profile from pole

to pole at several well-defined wavelengths, from the thermal infrared at 5 μm to the main methane absorption bands and their adjacent continuums. This was followed by soundings of Saturn's zonal wind profile until the present time.

Figure 4.13 summarizes the obtained zonal winds for Saturn from Voyager and Cassini data in optical wavelengths at the cloud-top level. Saturn shows an almost symmetric distribution of about six jet streams in each hemisphere. In contrast with Jupiter, Saturn's equatorial jet is more intense and broader, with wind speeds that reach 400 m s^{-1} at the ammonia cloud level (~500 mbar) according to measurements derived from Cassini data since 2005 (García-Melendo et al., 2011b). Measurements made during the Voyager flybys reveal that the equatorial jet was possibly stronger then, with a peak velocity close to 500 m s^{-1}. Saturn's wind distribution has other unique features not found in Jupiter's zonal wind system. While both planets have similar broad eastward equatorial jets with a double symmetric peak structure, Saturn's equatorial jet is more complex with the presence of an equatorially centered, narrow-peaked jet that increases in intensity with altitude (García-Melendo et al., 2010). While the broad equatorial superrotation drops from ~400 m s^{-1} at the ammonia cloud top deck (500 mbar) to 300 m s^{-1} at the tropopause at 60 mbar between ±20° around the equator, the narrow equatorial jet increases its strength from 380 to 440 m s^{-1} and might also be connected to a high-altitude stratospheric jet (Li et al., 2008). Temporal variability and strong vertical shears have been reported recently (Sánchez-Lavega et al., 2016). This indicates that the equatorial dynamics of Saturn is more complex than that of Jupiter. Vertical wind shear was also detected at other jet peaks at mid-latitudes, but with lower intensity due to the smaller pressure difference identified by the Cassini narrow-band filters (between 100 mbar and 350 mbar; García-Melendo et al., 2009). Another distinctive characteristic of Saturn's zonal wind system is the presence of two strong vortices centered at the poles with maximum wind speeds of ~120 m s^{-1} (north) and ~160 m s^{-1} (south) at ±88° (Sánchez-Lavega et al., 2006; Dyudina et al., 2008; Baines et al., 2009; Antuñano et al., 2015; Sayanagi et al., 2017). The South Polar Vortex (SPV) presents an eye free of clouds and a warm core mimicking some aspects of a terrestrial hurricane (Dyudina et al., 2008).

4.7.2 Middle Cloud Level

Below the main upper cloud, wind measurements are more scarce. Cassini VIMS data at 5 μm are especially useful here because of its potential to probe deeper layers of the atmosphere. At 5 μm, Saturn's deep atmospheric cloud features are seen "backlit" against the infrared emission, indicating that these features are located anywhere in between the top of the atmosphere and the 5 μm emission level. At this wavelength, cloud opacity is dominated by the NH_4SH cloud located at the 2–4 bar altitude level (Baines et al., 2005; Momary et al., 2006), whereas the emission level is close to 5 bar (Bjoraker et al., 2007).

Choi et al. (2009) undertook an analysis of VIMS data of the Saturnian atmosphere from Cassini and adapted an automated cloud feature tracking algorithm to construct the zonal wind profile of Saturn's atmosphere from VIMS data (Fig. 4.14).

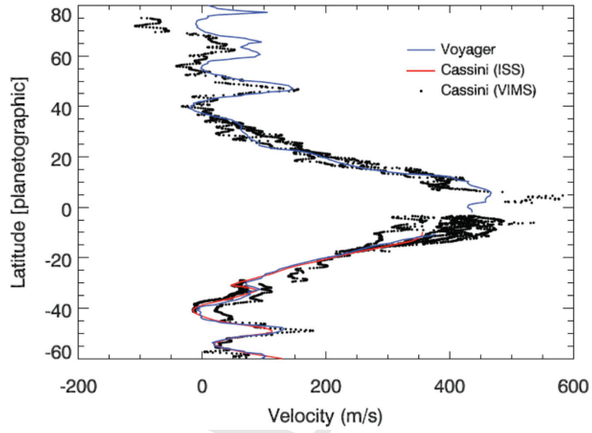

Figure 4.14 Scatter plot of zonal wind velocity vs latitude for Saturn's atmosphere constructed from VIMS data (Choi et al., 2009). For comparison, two other profiles are shown: the blue line is from Voyager images (Sánchez-Lavega et al., 2000), and the red line is from Cassini ISS images (Vasavada et al., 2006). Uncertainties for the VIMS measurements are ±10 m s^{-1}, and are dependent on the amount of latitudinal wind shear.

Generally, the zonal wind profile from 5 μm VIMS data is roughly in agreement with the jet location and magnitude of previous zonal wind profiles from Voyager and Cassini, but many substantial local differences appear at low and high latitudes.

VIMS images provide evidence for rapid equatorial flow at the jet core: clouds just north of the equator flow at ~500 m s^{-1}, and perhaps even faster. This suggests that the near factor-of-two reduction in speed relative to Voyager measurements for the equatorial jet could be confined to the upper troposphere, and that VIMS may be sensing deeper levels of the jet at these latitudes. However, some caution is needed with measurements of rapid flow at the jet core (i.e. the cluster of points with $u > 500$ m s^{-1} at ~1–5° N and 7° S), as the equatorial region typically lacks discrete high-contrast cloud features. Choi et al. (2009) noted that it is possible that the highest speeds could correspond to a local disturbance and may not be characteristic of the zonally averaged flow. It seems clear that the equatorial jet speed exceeds ~400–450 m s^{-1} at the pressure sensed by VIMS 5 μm images.

At higher latitudes, jets in the VIMS data are in remarkably good agreement with zonal wind profiles of the upper clouds from Voyager and Cassini. However, differences exist in the peak speeds measured at the jet cores, with the exception of the jet near 45° N, where the derived speeds from VIMS are nearly identical to those from Voyager. Furthermore, there is no universal increase or decrease of the peak velocities across all jets between VIMS and the other wind profiles. The jet cores at 75° N and 50° S appear to be flowing faster than in the previous profiles. The measurement at 75° N is attributed to a cluster of clouds located north of a large dark spot feature, and these clouds appear to be embedded in a relatively wide westward-flowing jet. At 50° S, a cloud feature that is embedded in a dark stripe (presumably corresponding to a narrow jet stream) is the likely source for the VIMS measurement. It is unclear how closely the motion of these features represent the ambi-

ent zonally averaged zonal flow. The measurement at 60° S also supports the presence of apparent wind shear compared with past profiles, though this measurement is less convincing from the lack of repeat observations. One of the starkest differences between the VIMS zonal wind profile and previous profiles is the jet at 65° N, which appears to be flowing at nearly half of the speed of the jet at that latitude as seen by Voyager.

Using information gleaned from the ISS and VIMS zonal wind profiles, and assuming that they originate from different depths, constraints about the latitudinal temperature gradient of Saturn's atmosphere can be obtained. Choi et al. (2009) assumed that the features tracked by ISS and VIMS are separated by a scale height. By using an uncertainty estimate of $\pm 10\,\mathrm{m\,s^{-1}}$ for the winds at both levels, they estimated an upper bound of ~0.5 K/1000 km for $\partial T/\partial y$. When extrapolated over 5000–10 000 km, the zonal wind profiles rule out latitudinal temperature contrasts exceeding 2–5 K throughout most of the atmosphere.

However, apparent wind shear is present at certain jet cores. Faster wind speeds are found at deep levels at the equator and at the 48° S jet core. Sánchez-Lavega et al. (2007) used methane and near-infrared filter images from Cassini ISS and observed higher-altitude features flowing at a slower speed compared to features at the main cloud deck (~700 mbar), yielding a vertical wind shear $\partial u/\partial z \sim 40\,\mathrm{m\,s^{-1}}$ per atmospheric scale height H (~50 km at the equator). García-Melendo et al. (2009) extended that work to show that vertical wind shear (estimated at $10\,\mathrm{m\,s^{-1}}$ per atmospheric scale height H) is present at several southern hemisphere zonal jets (see also Sánchez-Lavega et al., 2016). However, if the features tracked by ISS and VIMS are separated by a scale height, the $\sim 100\,\mathrm{m\,s^{-1}}$ difference at the jet cores implies a shear that is greater than the estimate from Sánchez-Lavega et al. (2007) by a factor of 2–3. The wind shear implied by Choi et al. (2009) is also well above the $\sim 25\,\mathrm{m\,s^{-1}}$ per atmospheric scale height at the 500 mbar level estimated from CIRS thermal data by Flasar et al. (2005).

4.7.3 Winds Above Clouds

Cloud features detected in broadband images in the visual range are located at approximately the same altitude (although this depends on latitude). A mean altitude pressure level of 750 mbar can be considered as a reference for both planets (West, 2004), and differences in cloud tops for different features span much less than one scale height (H). However, at ultraviolet wavelengths (250–350 nm) and in the deep methane absorption bands (890 nm and 2.3 μm), the upper hazes dominate the visual aspect of the planet. Tracking the motions of discrete features in these images allows direct measurements of the zonal winds up to a scale height above the main cloud deck and evaluation of the vertical shear of the zonal wind $\partial u/\partial z$ (Sánchez-Lavega et al., 2007; Li et al., 2010; García-Melendo et al., 2011b). Additionally, tracking of the debris left at higher altitudes by large impacts in Jupiter's atmosphere in 1994 (Sánchez-Lavega et al., 1995) and 2009 (Sánchez-Lavega et al., 2010) have been used to derive the zonal and meridional components of the wind above the main cloud up to 20 mbar altitude level.

In the absence of detectable particles in the stratospheres and upper atmospheres of the giant planets, zonal winds at these altitudes can be estimated by applying the thermal wind equation using knowledge of the meridional variability of temperatures and the wind profile at the cloud level. Since Jupiter's and Saturn's winds are in geostrophic balance (Ro $\ll 1$), the vertical shear of the horizontal wind speed is related to the horizontal temperature gradients by the thermal wind equation:

$$-\frac{\partial v_g}{\partial p} = \frac{R}{pf}\hat{k} \times \vec{\nabla}_p T \tag{4.6}$$

where v_g is the geostrophic wind, p is pressure, R is the specific gas constant, f is the Coriolis parameter and T is the temperature. For purely zonal motions in hydrostatic equilibirum this equation takes the form

$$f\frac{\partial u}{\partial z} \approx -\frac{g}{T}\frac{\partial T}{\partial y}. \tag{4.7}$$

Thus, except for a narrow band near the equator where the geostrophic approximation breaks down, measurements of the meridional temperature gradient above the upper cloud layer allow us to determine the vertical structure of the geostrophic wind from the ~1 bar altitude level (where the measured wind profile from cloud tracking is used as reference) to the 1 mbar altitude level. From the thermal wind equation and thermal data from the IRIS instruments on the Voyagers (Gierasch et al., 1986; Magalhaes et al., 1990) and the CIRS instrument on Cassini (Flasar et al., 2004a, 2005; Simon-Miller et al., 2006; Li et al., 2008), the zonal wind structure of Jupiter and Saturn should largely decay some 3–4 scale heights above the level of the cloud-tracked winds (Fig. 4.15).

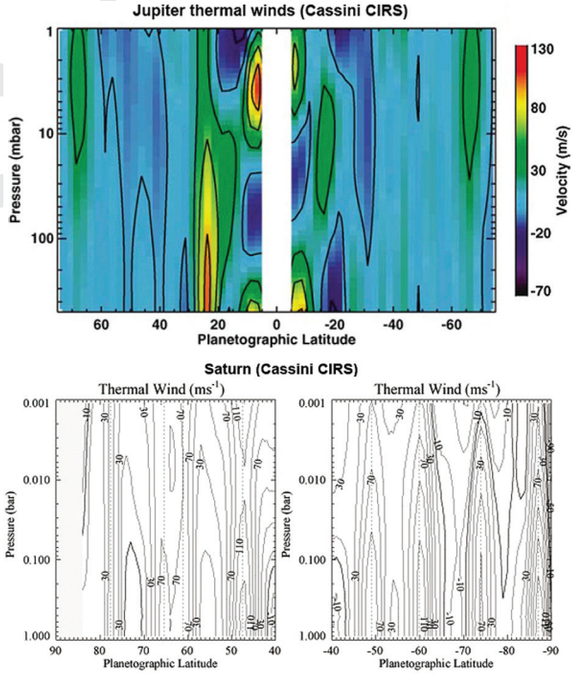

Figure 4.15 Vertical meridional cross-section of Jupiter's thermal wind (upper panel) and Saturn's thermal winds above cloud-top level in the northern (left) and southern (right) hemispheres. Jupiter map from Simon-Miller et al. (2006); Saturn maps courtesy of L. N. Fletcher (JPL/Oxford University) and the Cassini CIRS team.

Several two-dimensional radiative–convective models have been used to calculate the long-term meridional flow in the stratospheres of the giant planets. Conrath et al. (1990) calculated stratospheric heating through absorption of solar radiation by CH_4 gas alone. They predicted that the residual mean circulation, also known as the diabatic circulation, in the stratospheres of all the giant planets would consist of air rising over the sub-solar latitude and descending over the poles. For all the giant planets except Jupiter, whose obliquity is very small, this implies that the latitude corresponding to the location of rising air would be seasonally dependent. West et al. (1992) considered additional heating by absorption of ultraviolet sunlight by stratospheric hazes near Jupiter's poles. In their model, air rises over the poles above the 10 mbar level and descends at the equator. At lower altitudes, air descends over both poles. This model thus predicts equatorward motion above the 10 mbar level and poleward motion below this level. Another study, by Moreno and Sedano (1997), used revised haze and methane absorption models to yield a meridional flow structure closer to those of Conrath et al. (1990). Clearly these models are highly dependent on the properties and distribution of absorbing gases and hazes. Thus, we would expect a similar sensitivity to gases and hazes for Saturn, but less so for Uranus and Neptune, which do not have significant UV-absorbing polar hazes.

The deposition of particles into the stratosphere and upper atmosphere of Jupiter by the collision of several fragments of Comet Shoemaker–Levy 9 in 1994 provided an unexpected chance to trace circulation high above its tropospheric cloud deck (Sánchez-Lavega et al., 1995; Beebe, 1996). All of the models of Jupiter's atmosphere discussed above predicted poleward motion of air between the 10 and 100 mbar pressure levels, with cometary debris at the 45° S impact latitude expected to drift southward (Friedson et al., 1999). Instead it drifted toward the equator, reaching a latitude of 20° S by 1997 (Sanchez-Lavega et al., 1998a), and trace gases introduced by the impact drifted past the equator (Lellouch et al., 2002).

Detailed summaries of stratospheric and upper-atmospheric circulation are given by Irwin (2009) and recent reviews of Jupiter's atmospheres by Ingersoll et al. (2004) and Moses et al. (2004) and of Saturn's atmosphere by Del Genio et al. (2009).

4.7.4 Deep Winds

We have almost no direct information about the vertical structure $u(z)$ of zonal winds for the two gas giants Jupiter and Saturn. The only direct experimental result was obtained by the Galileo Probe Mission on July 13, 1995, which entered Jupiter's atmosphere at a planetographic latitude of 7.5° N and sent information, among other magnitudes, of Jupiter's vertical wind structure down to the 21 bar level (Atkinson et al., 1998); see Fig. 4.16. Measurements indicated that at that latitude, Jupiter's zonal wind speed increased up to 180 m s^{-1} at 5 bar, but then it remained more or less constant down to 21 bar. It is not clear whether these results are representative of the vertical wind shear at other Jupiter latitudes. The atmospheric probe was released into a 5 μm hot spot, a particular region dominated by the presence of a planetary-scale Rossby wave. Numerical experiments suggested that wind measurements may be affected by the presence of the Rossby wave and therefore it is not representative of the whole planet (Showman and Dowling, 2000).

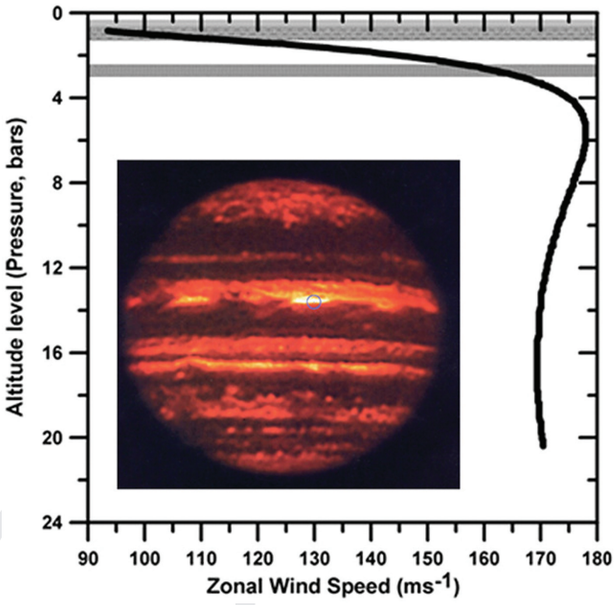

Figure 4.16 Vertical profile of the wind speed as measured by the Galileo probe (Atkinson et al., 1998) that entered a "hot spot" region – the circle in the bright area in the inset image (Orton et al., 1996).

Indirect evidence of slightly increasing winds under the cloud tops, in the upper tropospheres of Jupiter and Saturn, are given by observation of planetary-scale convective storms. These are supposed to originate at the water cloud level at ∼6 bar on Jupiter (Hueso and Sánchez-Lavega, 2001), and ∼10 bar on Saturn (Hueso and Sánchez-Lavega, 2004). Simultaneous knowledge of Jupiter's and Saturn's wind profiles and storm dynamics at the times of different planetary-scale disturbances (the 2007 North Temperate Belt Disturbance on Jupiter and the Saturn 2010 Great White Spot; Sánchez-Lavega et al., 2008a, 2011) suggest that winds at the water cloud level moved, in absolute terms, about 10 m s^{-1} faster than those at the cloud-top level (Fig. 4.17).

Further exploration of the vertical $u(z)$ structure in the weather layer can be performed by numerical modeling of the dynamical interaction between the cloud-top atmosphere and meteorological features that extend in depth like planetary-scale storms and large-scale vortices for both Jupiter (García-Melendo et al., 2005; Legarreta and Sánchez-Lavega, 2008; Sánchez-Lavega et al., 2008a; Morales-Juberias and Dowling, 2005) and Saturn (García-Melendo et al., 2007, 2013; del Río-Gaztelurrutia et al., 2010; Sánchez-Lavega et al., 2011). For this purpose, the dry-air global circulation EPIC model (Dowling et al., 1998) has been intensively used. For an adiabatic atmosphere like in the EPIC model, potential vorticity (PV) is conserved following the motion of fluid parcels. In many simulation experiments, PV has been successfully used as a proxy for the observed small-scale structure of the visible cloud-top ammonia clouds. The vertical structure of the zonal winds does not need to be uniform at all latitudes for both giant planets, but most numerical experiments are able to

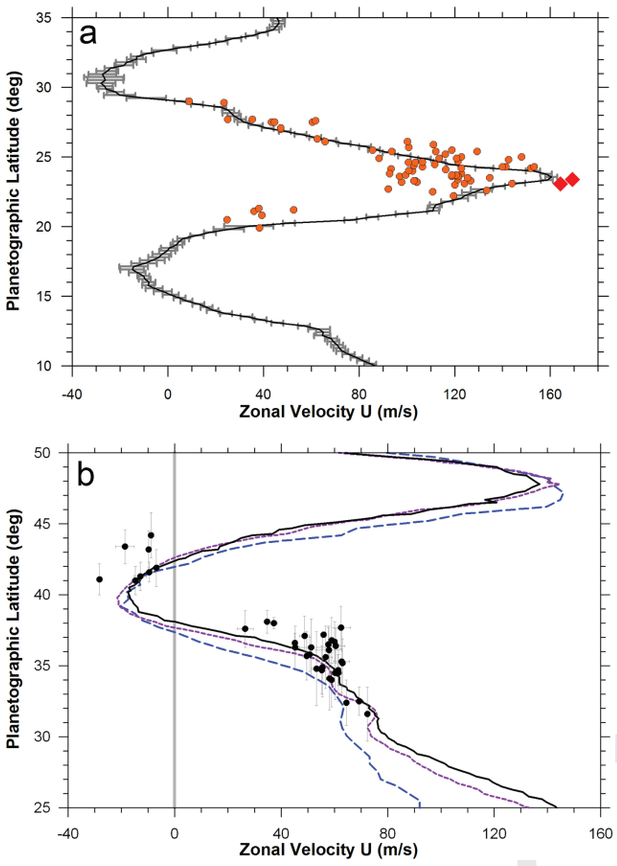

Figure 4.17 Zonal velocity of the convective storm plumes in (a) Jupiter's 2007 NTBD (Sánchez-Lavega et al., 2008a) and (b) Saturn's 2010 GWS (Sánchez-Lavega et al., 2011). Different lines correspond to the zonal wind profile for different periods of time following the evolution of the planetary-scale storm.

correctly reproduce the observed morphology and dynamics. In the case of Jupiter, good results are obtained with non-decaying winds well below the solar penetration level in most simulation experiments, whose magnitude ranges between $\sim 4\,\mathrm{m\,s^{-1}}\,H^{-1}$ and $\sim 15\,\mathrm{m\,s^{-1}}\,H^{-1}$ at 6 bar, depending on the point of the zonal wind profile being considered. In the case of Saturn, simulations agree on constant or slightly decaying winds between 0.5 bar and 10 bar, when vortices or the 2010 GWS storm are simulated (see references above). In all these cases vertical wind shear is about $-5\,\mathrm{m\,s^{-1}}\,H^{-1}$, and depends on the latitude being considered. Nevertheless, the wind may be slightly increasing with depth at the jet peaks, as suggested by numerical works by Sayanagi and Showman (2007) and Sayanagi et al. (2010b).

4.8 JUPITER AND SATURN: EDDY WIND COMPONENTS AT CLOUD LEVELS

The zonal jets on Jupiter and Saturn are the result of the competition between processes that supply momentum to and remove momentum from the jets. The jets are remarkably stable over long time intervals (Section 4.9), implying that momentum sources and sinks are in approximate balance. Modeling studies have suggested a variety of physical mechanisms by which the jets might be maintained. These include momentum transport by the mean meridional circulation and by covariances between instantaneous local fluctuations ("eddies") in the zonal wind and the meridional or vertical wind components.

Deviations of instantaneous horizontal zonal (u') and meridional (v') wind velocities from the zonal mean were first retrieved for Jupiter's visible cloud levels from manual tracking of cloud features in Voyager 1 and 2 flyby images by Beebe et al. (1980), Ingersoll et al. (1981) and Mitchell (1982). Eddy zonal and meridional wind speeds were 10–20 $\mathrm{m\,s^{-1}}$ and 5–10 $\mathrm{m\,s^{-1}}$ in the zonal and meridional directions, respectively. The zonal mean covariance $\langle u'v' \rangle$, indicative of the horizontal momentum transport, was found to be positively correlated with the latitudinal shear of the mean zonal wind $\mathrm{d}\langle u \rangle / \mathrm{d}y$, indicating that eddies transport momentum into the eastward jets and out of the westward jets. Sromovsky et al. (1982) raised questions about this result because of human target selection bias and the presence of outlier wind vectors that may have contributed disproportionately to the covariance. Salyk et al. (2006) made use of images from the Cassini flyby of Jupiter and an automated cloud tracking program to revisit these questions. The automated technique dramatically increases the number of vectors and provides a less biased sample. Several tests were run to remove potential sources of bias, and concluded that none of these significantly affect the result, lending confidence to the conclusion that eddies supply momentum to Jupiter's jets. For an assumed 2.5 bar depth of the weather layer (see Fig. 4.2), Salyk et al. (2006) found that the rate of conversion of eddy to zonal mean kinetic energy was 0.7–1.2 $\mathrm{W\,m^{-2}}$, about 5% as large as Jupiter's thermal energy flux to space. By comparison, the eddy–zonal energy conversion rate on Earth is only about 0.1% of its emitted thermal flux (Ingersoll et al., 1981).

Saturn has been a more difficult target for observations of tropospheric dynamics because of its thick upper tropospheric haze (Karkoschka and Tomasko, 2005; Pérez-Hoyos et al., 2005), which limits feature contrasts at deeper levels and thus results in fewer reliable targets to track than for Jupiter. Several unsuccessful attempts to derive eddy momentum fluxes with a small sample of manually tracked wind vectors in visible wavelength images were made with the Voyager Saturn dataset (Ingersoll et al., 1984; Sromovsky et al., 1986). However, the Cassini ISS instrument (Porco et al., 2004) carried near-infrared continuum filters that permitted better partial seeing through the Saturn haze to the ammonia cloud-top level (Section 4.4.1). These filters reduce the contribution of Rayleigh scattering and thus improve the contrast of features at higher levels. Using an automated tracking technique, this allowed an order of magnitude more wind vectors, with relatively unbiased sampling, to be obtained for Saturn than had been the case for Voyager. Cassini Saturn data in the 750 nm continuum band showed that $\langle u'v' \rangle$ was positively correlated with $\mathrm{d}\langle u \rangle / \mathrm{d}y$, just as for Jupiter, but with about half the energy conversion rate estimated for Jupiter (Del Genio et al., 2007; Del Genio and Barbara, 2012); see Fig. 4.18.

Del Genio and Barbara (2012) found that the $\langle u'v' \rangle$ source for jet momentum and the corresponding energy convergence rate are larger for the eastward jets than the westward jets. Furthermore, by tracking features in 727 nm methane absorption

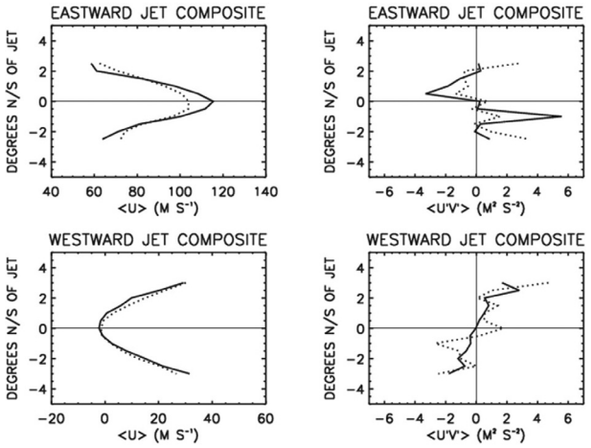

Figure 4.18 Composite latitudinal profiles of mean zonal wind and eddy momentum flux for three eastward jets and four westward jets on Saturn (Del Genio and Barbara, 2012). The solid curves are from continuum filter images that sense the mid-tropospheric ammonia cloud level, and the dotted curves are from methane absorption band images that sense the upper troposphere.

band images, which sense features several hundred millibars higher up in the upper troposphere haze, they demonstrated that the eastward jets weaken and broaden upward, accompanied by a weakening of $\langle u'v' \rangle$, as expected for eddy-driven jets (e.g., Dritschel and McIntyre, 2008). No similar vertical variation is seen in the westward jets. This is consistent with the staircase latitudinal profile of potential vorticity derived by Read et al. (2009), with the "steps" at the eastward jet cores where air mixed from opposite sides of the jets meets. The decrease in $\langle u'v' \rangle$ upward on Saturn suggests eddies that are driven at or below the continuum cloud level, perhaps by a process such as baroclinic instability, as suggested by Godfrey and Moore (1986). However, models simulating such instabilities are not yet able to reproduce propagation characteristics of observed wave-like features such as the ribbon wave (Sayanagi et al., 2010b) – Fig. 4.8 – and the relative roles of baroclinic and barotropic conversion have yet to be determined. The magnitude of the implied energy conversion rate severely limits the depths of the eddies, seemingly ruling out a deep convective cylinder source for at least the extratropical jets (Liu and Schneider, 2010). The upward decrease in $\langle u'v' \rangle$ also seems to rule out radiative driving for Saturn, where solar heating is concentrated in the upper tropospheric haze (Pérez-Hoyos and Sánchez-Lavega, 2006b). Driving by differential insolation as suggested by Liu and Schneider (2010) may be more tenable for Jupiter, where there is no thick haze and sunlight penetrates deeper.

In the absence of radiative driving, the most likely energy source for the eddies maintaining the jets may be lateral temperature contrasts due to the latent heat released by water condensation (Lian and Showman, 2010), although many aspects of this idea remain to be fully explored. On Jupiter, and to at least some extent on Saturn, deep convective clouds are most common in the cyclonic shear zones (Ingersoll et al., 2000; Porco et al., 2003; Del Genio et al., 2007), implying that these are regions of moisture convergence near the deep water condensation level, positive deep temperature anomalies and net large-scale rising motion above. This then implies that the mean meridional circulation is thermodynamically indirect, with rising poleward of the eastward jets, sinking equatorward of the jets, and an equatorward mean meridional flow $\langle v \rangle$ in the upper branch of the mean circulation. The Coriolis force on this meridional flow may then be the momentum sink that balances the eddy source, i.e., to first order, $-f\langle v \rangle = -\mathrm{d}\langle u'v' \rangle / \mathrm{d}y$, where f is the Coriolis parameter. The meridional wind required to maintain this balance ($\sim 0.02\,\mathrm{m\,s^{-1}}$) is much smaller than that detectable in cloud-tracked winds (Del Genio et al., 2007).

4.9 JUPITER AND SATURN: TEMPORAL VARIABILITY OF WINDS

Overall, the zonal jet systems of Jupiter and Saturn have been stable since the beginning of detailed spacecraft observations. Some changes have been detected in the intensity of a few jets in Jupiter and Saturn, but not in their latitudinal location. A large part of the detected variations may be due to vertical wind shear and variations in the pressure level of the clouds used as wind tracers.

In the case of Jupiter, Simon-Miller et al. (2000) performed a systematic search of Voyager, HST and Cassini wind data for periodicities in the jet wind velocities, but found only a few latitudes with potential variability near the equator at 0° at 10–12° N and at 14–28° S planetographic latitudes, but inad-

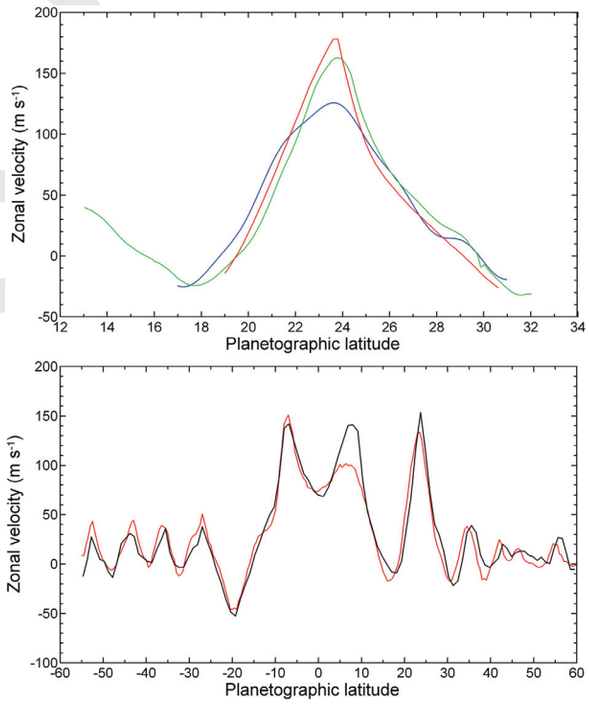

Figure 4.19 Upper panel: Changes in the 24° N Jovian jet between 1979 and 1997. Voyager measurements are in red (Maxworthy, 1984) and green (Limaye, 1986); HST measurements in the 1994–97 period appear in blue (García-Melendo et al., 2000). Lower panel: Apparent variability of Jupiter's equatorial jet symmetry for 1994–98 (black line; García-Melendo et al., 2000) and 2011 (red line; Barrado-Izagirre et al., 2013), possibly due to the respective presence (1994–98) or absence (2011) of a trapped Rossby wave.

equate temporal coverage did not allow good interpretation of the data. More robust changes (without a clear asssociated periodicity) have been detected in the the 24° N eastward jet and in the North Equatorial Belt at 7° N. In the first case, intensity fluctuations go from 180 m s^{-1} at the time of the Voyagers (Maxworthy, 1984) to 120 m s^{-1} in modern times (Simon, 1999; García-Melendo et al., 2000); Fig. 4.19. These changes of the jet peak speed are associated with morphology changes and large-scale convective disturbances that cause considerable turbulence and might develop hydrodynamic instabilities (García-Melendo et al., 2000; Barrado-Izagirre et al., 2009; Tollefson et al., 2017). However, the general structure of the jet did not change during these large-scale disturbances (Sánchez-Lavega et al., 2008a). Changes in the North Equatorial Belt in the north part of the equatorial jet have also been reported several times (Asay-Davis et al., 2011; García-Melendo et al., 2011a; Barrado-Izagirre et al., 2013). These changes are possibly not real but caused by the superposition of the true zonal wind with the motions of large-scale dark equatorial projections interpreted as the manifestation of an equatorially trapped Rossby wave moving with a certain phase speed (Allison, 1990; Arregi et al., 2006; García-Melendo et al., 2011a; Ortiz et al., 1998; Showman and Dowling, 2000).

For Saturn, the most conspicuous change is found in the equatorial jet. During the Voyager encounters in 1980–81 the jet reached peak velocities of ~480 m s^{-1} in green-filtered images (Ingersoll et al., 1984; Sánchez-Lavega et al., 2000). When the zonal wind profile was measured in high-resolution HST images in the 890 nm methane-band filter (1994–2000), maximum velocities were 200 m s^{-1} slower (Sánchez-Lavega et al., 2003). Analysis of Cassini ISS observations in the 890 nm methane band and the adjacent continuum were able to sense pressure levels of 60 mbar and 300 mbar respectively, detecting a vertical wind shear of 100 m s^{-1} between both levels and partially explaining the difference (Porco et al., 2005; Vasavada et al., 2006; García-Melendo et al., 2011b). However, the wind speed at 300 mbar was 100 m s^{-1} slower than Voyager measurements. Voyager images sounded the ~300–400 mbar levels (Pérez-Hoyos and Sánchez-Lavega, 2006b), but some cloud features used as tracers in Voyager images might be rooted at deeper levels. In fact, thermal infrared measurements with the Cassini VIMS instrument suggest that winds may increase by 100 m s^{-1} below the 2 bar level (Choi et al., 2009). The 1990 Great White Spot (Sánchez-Lavega et al., 1991) might have affected the equatorial jet at the visible ammonia cloud level (Sánchez-Lavega et al., 2003; Sayanagi and Showman, 2007). It has recently been shown that strong vertical shear and temporal variability occurs at Saturn's equator (Sánchez-Lavega et al., 2016).

4.10 WINDS OF URANUS AND NEPTUNE

The atmospheres of Uranus and Neptune have comparatively simple circulations, both highly zonal and each characterized by a broad retrograde equatorial jet and high-latitude prograde jets. The circulations are surprisingly similar considering their very different spin-axis inclinations and internal heat sources, and their winds surprisingly strong considering their weak absorbed flux of sunlight. Their circulations have been measured mainly by tracking discrete cloud features, with some additional constraints provided by radio and stellar occultations. Discrete cloud features provide the most detailed information about atmospheric motions, but complicate our understanding by not always following the local mass flow. Examples of such behavior in the Earth's atmosphere are the orographic clouds in stationary waves formed by air flowing over mountain ranges (and through the clouds). A similar kind of cloud is thought to accompany large features on Uranus and Neptune, the most prominent of which is the Great Dark Spot (GDS) on Neptune, which had many "companion" clouds that moved at the same rate as the GDS, even though they were displaced by a significant distance in latitude. There is also a segregation of features by lifetime. Some features, especially on Neptune, do not even last for a complete revolution of the planet, while others, especially on Uranus, seem to last for decades. Another strange characteristic of these planets is that there is a great deal of small-scale latitudinal banding that seems to have no connection to any feature of the measured circulation. This is quite unlike Jupiter, for which cloud bands and zonal wind changes are strongly correlated. Although little is known about the weak mean meridional motions or eddy motions, the motions of discrete features are often not purely zonal. Oscillations in latitude and longitude of many features have been observed on both planets, some of which appear to be due to inertial oscillations, some possibly Rossby waves, and some appear to be related to meandering jet flow along streamlines stationary with respect to the interior.

Voyager visited Uranus in 1986, initially detecting only eight discrete cloud targets. It visited Neptune in 1989, finding an abundance of discrete cloud targets, large vortices and interesting dynamical phenomena. The clouds of Uranus were of very low contrast at the wavelengths available to the Voyager camera system, and details of its circulation had to be filled in many years later using primarily near-IR adaptive optics (AO) imaging by the Keck II telescope. HST imaging has also contributed to our knowledge of both circulations since 1994. A very recent reanalysis of Voyager imagery by Karkoschka (2015) uncovered many very low-contrast features that provided new details of the 1986 southern hemisphere circulation of Uranus that could not be characterized by ground-based observations. The circulation of Uranus appears to have a small, but persistent, mid-latitude hemispheric asymmetry, but a rather large high-latitude asymmetry. Polar motions are only known in the south polar regions of Neptune, because the north has remained hidden from view.

In the following, we first discuss measurements of the circulation of Uranus, followed by a similar discussion of measurements of Neptune. In each case we summarize the published observations, and discuss their relationship to each other. This is followed by a discussion of the vertical extent of the zonal jets on both planets, based on analysis of their gravitational fields.

4.11 ZONAL JETS OF URANUS

4.11.1 Uranus Wind Datasets

The first wind observations of Uranus (Smith et al., 1986) were based mainly on tracking features observed in Voyager 2

images of Uranus acquired during the 1986 flyby. All of these were measured in the southern hemisphere, which was pointed towards the Earth at the time of the flyby. The only point in the dark (at that time) northern hemisphere was obtained by radio occultation (Lindal et al., 1987). The single point obtained in the south polar region was from a very subtle feature in UV images, and the motion of that feature was inferred from the rotational displacements in a sequence of images required to maximize the contrast of that feature in the average of the displaced images. The remaining targets were seen best at longer visible wavelengths, and all were of low contrast. These and all subsequent winds were defined relative to a frame rotating with the adopted 17.24 hr period of Uranus (Seidelmann et al., 2002), which is based on radio measurements with an uncertainty of ±0.01 hr (Warwick et al., 1986).

The next big improvement in Uranus wind measurements (Karkoschka, 1998) was obtained from near-IR images obtained by the HST NICMOS instrument, which showed a number of cloud features that had high contrast at 1.6 μm. Some of these were visible in the northern hemisphere, as Uranus moved toward its 2007 equinox. Further additions were made by an analysis of HST observations through 2000 (Hammel et al., 2001), a remeasurement of 2003 Keck results (Hammel et al., 2005; Sromovsky et al., 2009), Keck results from 2003 and 2004 (Sromovsky and Fry, 2005), 2005 Keck results (Sromovsky et al., 2007) and 2006 Keck results (Hammel et al., 2009).

A significant addition was made by Sromovsky et al. (2009) from analysis of intensive observations carried out near the time of the 2007 equinox of Uranus, when clouds in the north polar regions of Uranus became visible at wavelengths where no clouds had ever been seen in the southern hemisphere. The 2007 observations were finally able to detect cloud features up to 70° N, and obtained precise wind measurements up to 62° N (planetocentric) latitude, for the first time showing the beginnings of a northern prograde jet peak with a speed near 250 m s^{-1}. Taking advantage of better views of the northern hemisphere and special high signal-to-noise observing techniques (Fig. 4.20), further additions to the Uranus wind database were made by Fry et al. (2012a), based on HST WFC3 observations, and by Sromovsky et al. (2012a,b, 2015), based on Keck and Gemini observations at near-IR wavelengths. This resulted in a much better characterization of the north polar jet and identified a region from the jet peak towards the pole that was in precise solid-body rotation.

A very significant recent addition to the Uranus winds database was made by Karkoschka (2015), who reprocessed 1986 Voyager 2 images of Uranus to remove artifacts and improve nonlinearity corrections, making it possible to average large numbers of images to greatly improve signal-to-noise ratios. This enabled detection and tracking of very low-contrast cloud features in the southern hemisphere of Uranus, filling in large gaps in latitude coverage.

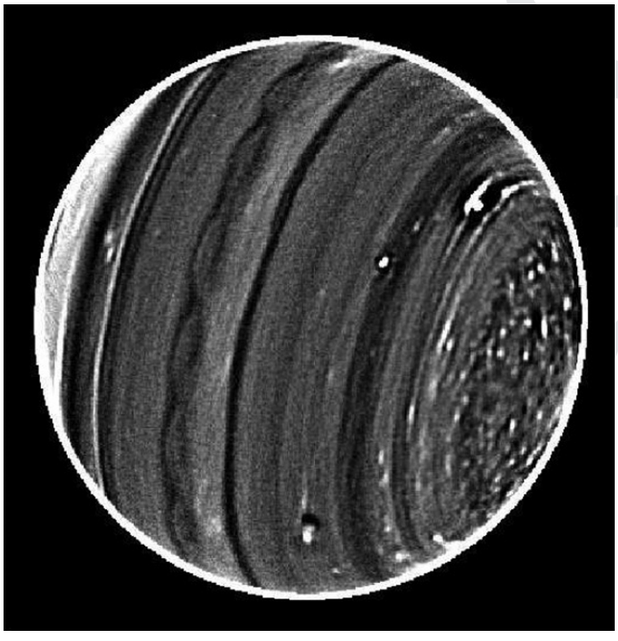

Figure 4.20 High signal-to-noise 2012 Keck II NIRC2 near-IR H-band (1.62 μm) image from July 25, 2012. Over 100 images were averaged and high-pass filtered after individual images were processed to remove planetary rotation and wind displacement between images (Fry et al., 2012b). The north pole is at about three o'clock. The scallops seen left of center are just south of the equator. For further examples from the 2012–2014 period see Sromovsky et al. (2015).

4.11.2 Uranus Zonal Wind Profiles

To provide a smooth profile, Sromovsky et al. (2012b) carried out Legendre polynomial fits to combinations of observations from 2009 and 2011, and also fitted a more extensive set of observations that included the highest-accuracy observations from 2007. They fitted the angular (longitudinal) drift rates rather than wind speeds because the observations are most consistent with a constant angular drift rate at high latitudes. They also added the 1986 Voyager measurement at 71° S (Smith et al., 1986) and artificial measurements of 4.3° hr^{-1} westward at both poles to better constrain high latitudes. The angular rate 4.3° hr^{-1} was chosen to match the nearest observed point. The Voyager point was not needed for fits that were constrained to be symmetric. Because both of these fits are more symmetric than the fit obtained to the 2007 data alone, the possibility that the circulation of Uranus is actually close to symmetric motivated them to carry out fits in which only the even Legendre polynomials were used, insuring fits that were symmetric about the equator. More recent zonal profile fits to 2012–2014 Keck and Gemini observations were provided by Sromovsky et al. (2015). These latter observations were consistent with a precise solid-body rotation rate of 4.1° hr^{-1} westward from 62° N to at least 83° N. Sromovsky et al. (2015) noted a discrepancy between near-equatorial motions of wave features and small discrete features, which moved eastward at 0.4° hr^{-1} and 0.1° hr^{-1} respectively. Sromovsky et al. (2015) provided three symmetric fits: one which combined all the new observations, one which excluded near-equatorial wave motions, and one which excluded near-equatorial discrete features and kept the wave motions. They also provided separate fits to asymmetry characteristics.

All these Legendre expansions were of the form

$$d\lambda/dt = \sum_{i=0}^{n} C_i \times P_i(\sin(\phi_g)), \tag{4.8}$$

where $P_i(\sin(\phi_g))$ is the ith Legendre polynomial evaluated at the sine of the planetographic latitude ϕ_g, $d\lambda/dt$ is the longitudinal drift rate in ° W hr^{-1} and the C_i are the coefficients tabulated for fits given by Sromovsky et al. (2009, 2012b, 2015). The drift rates are converted to wind speed using Eqs. (2.4) and (2.11), substituting the equatorial and polar radii of Uranus given by Archinal et al. (2011) as 25 559 km and 24 973 km, respectively. For the symmetric fits, the summation over i is only over the even polynomials. The model coefficients were found by minimizing χ^2, but with error estimates for the observations modified as described in the following paragraph.

Very accurate measurements of drift rates at nearly the same latitude often did not agree within their uncertainties, and often differed by many times the value expected from those uncertainties. Sromovsky et al. (2012b) offered several possible reasons: (1) the circulation is not entirely steady; (2) the measured features do not all represent the same atmospheric level; or (3) the tracked cloud features are not always at the same latitude as the circulation feature that is moving with the zonal flow. Examples of the latter possibility are the companion clouds to Neptune's Great Dark Spot, which traveled with the spot even though separated by nearly 10° in latitude (Sromovsky et al., 1993). Less extreme examples have also been seen on Uranus (Hammel et al., 2009; de Pater et al., 2011). If highly accurate measurements are included, and weighted by their estimated accuracy, they can dominate the fit, leading to unreasonable variations in regions where there are less accurate measurements. Since these high-accuracy measurements clearly do not all follow the mean flow, Sromovsky et al. (2012b) added an additional uncertainty to characterize their deviations from the mean flow. This was done by root-sum-squaring the estimated error of measurement with an additional error of representation. The size of the representation error was adjusted to make the χ^2 value of the complete asymmetric fit approximately equal to the number of degrees of freedom (number of measurements minus the number of fitted parameters). This representative error was approximately 0.1° hr^{-1} for both the 2009–2011 and 2007–2011 datasets. Sromovsky et al. (2015) obtained values between 0.125° hr^{-1} and 0.147° hr^{-1}, depending on which near-equatorial datasets were included.

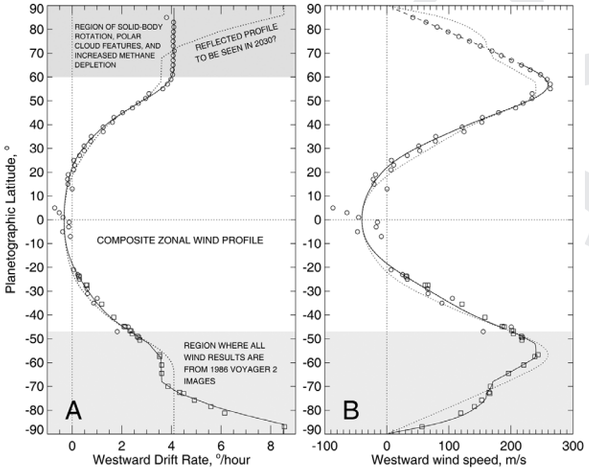

Figure 4.21 Adopted zonal wind profile (solid curve) from Sromovsky et al. (2015), which combines Keck results from 2012–2014 and new results from a reanalysis of 1986 Voyager images by Karkoschka (2015). The open circles are binned results of Sromovsky et al. (2015), the open squares are winds derived from discrete feature tracking by Karkoschka (2015), and the dashed line is the adopted profile reflected about the equator. Figure adapted from Sromovsky et al. (2015).

The current best estimate for the zonal wind profile of Uranus is the composite profile shown in Fig. 4.21 from Sromovsky et al. (2015). The profile was constructed starting with a symmetric ten-term Legendre fit (up to 18th order) to their 2012–2014 dataset, consisting of over 850 wind measurements sampling latitudes from 47° S to 85° N. To this they added a mid-latitude asymmetry function fitted to a dataset including observations back to 1997. For latitudes south of 47° S they adopted the same profile adopted by Karkoschka (2015), which is based on his reanalysis of 1986 Voyager images. This combination, shown as the solid curve in Fig. 4.21, is available in tabular form at 1° intervals (Sromovsky et al., 2015). The dotted curve is the reflection of the solid curve about the equator, revealing small mid-latitude and large high-latitude asymmetries between hemispheres. The open circles in the figure are the results of averaging the 2012–2014 results in 2° latitude bins. The dispersion of the binned results near the equator is a result of differences between the motions of waves and the motions of small discrete features.

4.11.3 Symmetry Properties

Sromovsky et al. (2012b) provided individual fits to the 2009 and 2011 datasets combined, and for the 2007, 2009 and 2011 datasets combined. They showed that these datasets alone cannot distinguish between symmetric and asymmetric models. They also combined the data from 1997 through 2005 (see Sromovsky et al., 2009, and references therein), selecting only those with wind errors $< 10\,\mathrm{m\,s^{-1}}$ and latitude errors $\leq 0.5°$, and then combined these with the high-accuracy winds from 2007–2011, which yielded a total of 125 observations (127, including synthetic polar points). A comparison of the asymmetry properties of the 2007–2011 observations and those of the earlier observations shows that the new fits are more symmetric than prior fits. Although the new observations make the entire dataset somewhat more symmetric, the remaining asymmetry is better defined. The 2012–2014 symmetry results of Sromovsky et al. (2015), shown in Fig. 4.22, don't change this picture very much. It is not clear whether the true asymmetry of the zonal winds has changed slightly or whether the new observations are just sampling a different statistical variation in target motions. The better definition of asymmetry obtained from the larger combined dataset depends on the earlier observations, which are better distributed in latitude and contribute more measurements in the southern hemisphere. The Berg feature is responsible for many of those observations; as it traveled from 33–34° S to 8° S (Sromovsky et al., 2009; de Pater et al., 2011) it provided samples of drift rates within that range, though unfortunately sampled too sparsely to provide a detailed profile. It

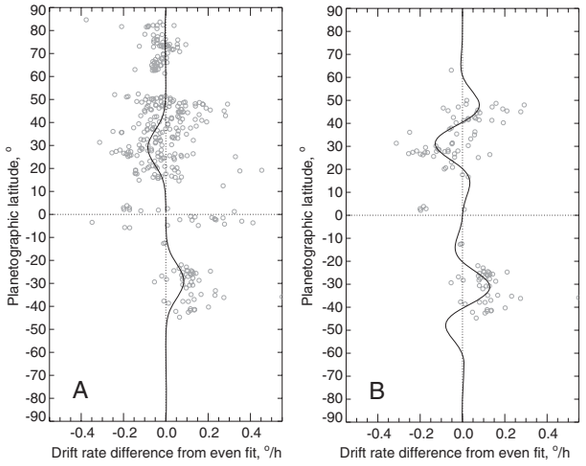

Figure 4.22 (A): Wind differences from a symmetric model fitted to high-quality wind observations from 1997–2014. (B) Differences that exclude observations from 2012–2014. Adapted from Sromovsky et al. (2015).

is clear that because high-accuracy winds do not always represent the mean zonal flow with similar accuracy, the asymmetry information in a sparsely sampled dataset can easily be misleading. With the large numbers of samples obtained by combining all observations from 1997 onward, this is less of a concern.

Combining observations between 1997 and 2005 with those up to 2011 provides an approximate representation of the circulation pattern near the 2007 equinox (the mean year of these observations is ~2006). If the asymmetry is actually a long-delayed seasonal effect (with a phase shift near 90°), then it should be reflected about the equator at the prior equinox, and near the midpoint of the transition in 1986, when Voyager observations were made. However, Sromovsky et al. (2012b) found that the 1986 Voyager measurements were not measurably different from their grand-average profile, nor from the 2007 equinox results alone (Sromovsky et al., 2009). This further enhances the probability that the mid-latitude asymmetry may be a relatively stable feature over a long period, perhaps more than a Uranian year. While this seems to violate our expectations of symmetry in the annual average (over the Uranian year), there are other examples of persistent asymmetry in zonal circulation profiles, namely those of Jupiter and Saturn.

Sromovsky et al. (2012b) also suggested alternative interpretations for the lack of change in asymmetry of the wind profile. For example, if the phase shift were closer to 45° and had a sinusoidal variation, then the asymmetry might be the same at both equinox and solstice, with maxima in between. Another possibility is that the symmetry variation does not proceed in a uniform or sinusoidal fashion, but achieves most of the change by the solstice, and changes little between solstice and the next equinox. Further observations over many years will be required to distinguish these possibilities.

The mid-latitude asymmetry pales in comparison to the dramatic high-latitude asymmetry revealed by the most recent wind results (Fig. 4.21). While the northern hemisphere has a broad region (from 62° N to at least 83°) of solid-body rotation (Sromovsky et al., 2015), the southern hemisphere has a much smaller region of solid-body rotation and much larger region of large gradients in drift rate (Karkoschka, 2015). Of course, the southern polar profile is what was present in 1986, while the northern profile is what was observed over 2012–2014. If this is a seasonal effect, then this combination is not an appropriate rendition of the current state of the Uranus circulation, and big changes in circulation might be observed between now and 2030, when the northern hemisphere will reach its next summer solstice and might be expected to attain at that time the circulation profile indicated by the dotted curve (a reflection of what was seen at the southern hemisphere's summer solstice).

4.11.4 Long-Lived Feature Tracking

Some cloud features on Uranus have extremely long lifetimes that permit studying motions on longer timescales. Karkoschka (1998) noted that over the 100-day period covered by his 1997 and 1998 NICMOS observations, all eight of the features he detected were visible whenever they were on the sunlit side of Uranus. A bright high-altitude cloud feature seen near 30° N (Sromovsky et al., 2007) was tracked for more than a year. The large "Berg" feature was observed to oscillate between 32° S and 36° S for many years, which it may have been doing since 1986, then observed to drift northward beginning in 2005 (Sromovsky and Fry, 2005; Sromovsky et al., 2009; de Pater et al., 2011), finally dissipating as it approached the equator near the end of 2009. Additionally, Sromovsky et al. (2009) were able to track eight features for well over a month (1055–2250 hr) during the intensive equinox observing period. Another long-lived bright feature near 30° N was tracked from July 26, 2011 until December 16, 2011 (Sromovsky et al., 2012a). More recently, Sromovsky et al. (2015) identified six long-lived discrete features that were tracked over time intervals of five months, more than a year, and more than three years. Most features move as if carried by the zonal mean flow. However, bright clouds associated with dark features appear to move as companions to dark features, following the zonal flow at the latitude of the dark feature. Several of these features exhibited equatorward drifts and some oscillated in latitude and drift rate.

4.11.5 Altitudes of Uranian Cloud Features

The most extensive set of effective cloud pressures were obtained from post-equinox observations in July and October of 2011 by Sromovsky et al. (2012b) using the spatial modulation technique. Most of the tracked cloud features were near the 1.2 bar methane condensation level or deeper. Several features in the northern hemisphere were found to be well above the methane condensation level, one reaching close to 400 mbar. According to Sromovsky et al. (2007), the brightest feature ever seen on Uranus reached estimated pressures near 300 mbar for its highest component, with other parts found between 400 mbar and 600 mbar. Another unusually bright feature, though much dimmer than the brightest feature, had estimated effective pressures ranging from 390 mbar to 690 mbar (Sromovsky et al., 2012a). During the same period a second bright spot was found at nearly the same latitude, but had a significantly higher effective pressure of 1–1.3 bar. The clouds comprising the Berg were investigated by de Pater et al. (2011). They found that the

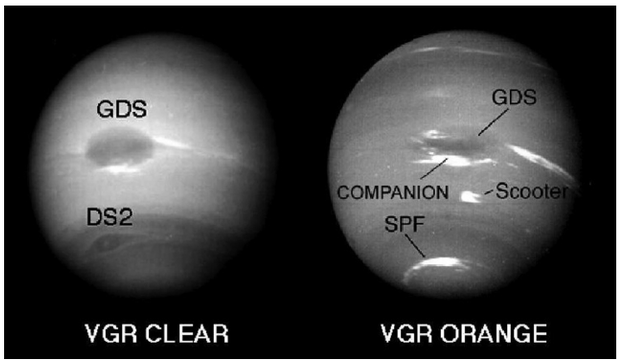

Figure 4.23 Voyager 2 images from 1989 of Neptune (north up) with clear and orange filters, illustrating major cloud features, of which only the SPF seems to still be present. Credit: NASA/JPL.

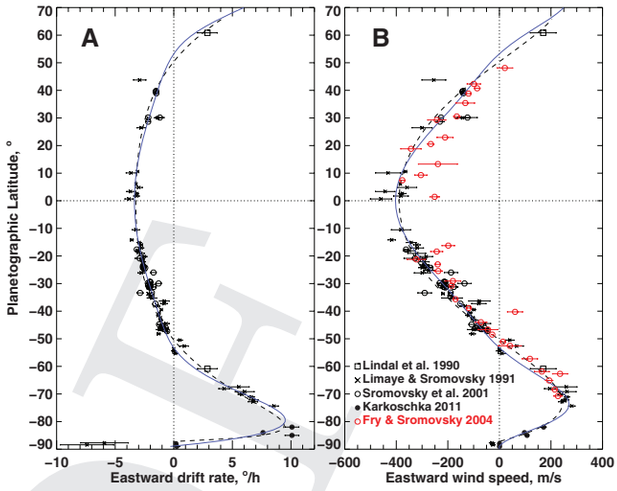

Figure 4.24 Neptune wind results from Voyager radio measurements (Lindal et al., 1990), cloud tracking in Voyager 2 images (Limaye and Sromovsky, 1991), cloud tracking in HST images (Sromovsky et al., 2001b), and recent work by Karkoschka (2011). The dashed curves trace the Sromovsky et al. (1993) sixth-order even fit to Voyager wind speeds. The solid blue curve is a new Fourier cosine series fit given in the text. The red open circles are from the binned results of Fry and Sromovsky (2004).

brightest parts of the feature, which is the only part of the feature that could be seen in K′ images, had effective pressures in the 550–750 mbar range, while the main part of the feature was much deeper, ranging from 1.7–3.5 bar.

4.12 ZONAL JETS OF NEPTUNE

4.12.1 Neptune Wind Datasets

The discovery of multiple periods in Neptune's light curve (Belton et al., 1981) strongly suggested that Neptune's winds varied with latitude. The first wind measurement based on discrete cloud tracking was made using ground-based methane-band images by Hammel and Buie (1987), although only one feature was visible in the low-resolution images that were obtained. Voyager 2 images acquired during its 1989 encounter with the planet provided the first detailed views of its fascinating cloud features. Neptune proved to be much more active than Uranus, generating many bright cloud features that were of decent contrast even over the limited wavelength range of the Voyager cameras. The first results, published by Smith et al. (1989), established the existence of the retrograde equatorial motions as well as a mid-latitude jet, but were somewhat misleading in two respects: (1) the largest wind speeds were obtained from unreliable cloud targets with large uncertainties, and (2) the motions of clouds in the region of the south polar feature were assigned the group velocity rather than the velocity of individual cloud features, which were not resolved in the early measurements. The follow-up paper by Hammel et al. (1989) fixed the first problem, but the second was not fixed until the more detailed analysis of high-resolution Voyager images by Limaye and Sromovsky (1991), which showed that the South Polar Features appeared nearly stationary at low resolution, but at high spatial resolution individual cloud elements were seen to form at one edge of the region of formation, move rapidly through that region, and dissipate as they exited the region. These clouds were also clouds that cast shadows, suggestive of strong vertical convection. This work provided what remains the most detailed wind dataset.

The Voyager wind results for Neptune are plotted as zonal drift rate in $^\circ\,\mathrm{hr}^{-1}$ vs planetographic latitude in Fig. 4.24A, and zonal wind speed in $\mathrm{m\,s}^{-1}$ in Fig. 4.24B. Other major datasets, to be discussed in the following, are also shown. These are all measured relative to a longitude system rotating with a period of 16.11 hr (Warwick et al., 1989), and conversion between longitudinal drift rate and wind speed assumes 1 bar radii of $R_\mathrm{E} = 24\,764$ km and $R_\mathrm{P} = 24\,341$ km (Lindal et al., 1990). These are consistent with the current IAU working group recommendations (Archinal et al., 2011). The two fits shown were to the zonal wind speeds to avoid the extremely sharp change in angular rates near the south pole. The dashed curves are from Sromovsky et al. (1993); the solid curves fit the observations using a cosine series expansion of the form $U(\phi) = \Sigma_{i=1}^{8} C_i \cos(i\theta)$, where θ denotes planetographic latitude and $C = [4139.5488, -13\,797.876, 20\,514.559, -20\,444.367, 14\,329.830, -6936.2231, 2081.4494, -289.73850]$ in units of $\mathrm{m\,s}^{-1}$. This fit was forced to nearly zero wind speed at the south pole by adding artificial points of zero wind speed at both poles and providing very high weights by assigning very low errors. It also added a representativeness error of $20\,\mathrm{m\,s}^{-1}$ to reduce the impact of very accurate long-term tracking results (see the discussion of Uranus error modifications). This fit did not include constraints from any recent Keck observations.

Additional work with the Voyager imaging data by Sromovsky (1991) and Sromovsky et al. (1993) identified a number of long-lived features that had cyclical latitudinal motions and variable longitudinal drift rates. The Great Dark Spot (GDS) drifted in latitude and varied its longitudinal drift rate to roughly, but not exactly, match the mean zonal wind profile inferred from tracking small-scale features. A smaller dark spot (DS2) oscillated in latitude and longitude, and also followed a variable drift rate that deviated somewhat from the mean zonal wind profile. The latitudinal excursions of these two dark spots trace out a zonal speed profile that seems to be an

attenuated version of that established by tracking small cloud features. One interpretation, that these are wave features generated by (and moving with) circulation features at deeper levels of the atmosphere, contradicts the inference from Voyager IRIS observations that the zonal winds decline with altitude rather than increase, although IRIS senses much higher altitudes than reached by either the small or large cloud features that were tracked.

An especially interesting result obtained by Sromovsky et al. (1993) is that the region of South Polar Feature (SPF) formation and the central longitude of the DS2 oscillation, though separated by 20° of latitude, remain at opposite sides of the planet in phase-locked synchronous rotation. Because of the long period of observation, this complex had a very well-defined rotation rate of 15.9699±0.0002 hr, based mainly on the more accurate DS2 observations. This is 200 times more accurate than the initial determination of the radio period of 16.11±0.05 hr (Warwick et al., 1989). It seemed unlikely that these two structures could be phase-locked unless they were both connected to the interior, leading Sromovsky and Limaye (1992) to suggest that their joint rotation might be a better rotation period of the interior than the radio period itself. However, the difference between the two periods was several times the uncertainty in the radio period of Warwick et al. (1989) and nearly 23 times the uncertainty in the revised period of Lecacheux et al. (1993). It was not until Saturn's radio period appeared to vary (Gurnett et al., 2005) that this idea was given new life by Karkoschka (2011), which will be discussed later.

Early observations by the Hubble Space Telescope in late 1991, before the spherical aberration was corrected, produced the first post-Voyager additions to the circulation of Neptune. Sromovsky et al. (1995) were able to identify and track eight discrete cloud features, most of which were quite consistent with the Voyager wind profile. After the spherical aberration was fixed, HST observations became more prolific. Hammel and Lockwood (1997) analyzed HST images obtained in 1994, 1995 and 1996, finding dark spots in 1994 and 1995, and bright spots at latitudes where none had previously been seen, which made it possible to fill in some gaps in the Voyager profile. From 1995 HST data they obtained wind speeds from six long-lived features, three of which were at new latitudes. Sromovsky et al. (2001a) analyzed HST observations from 1996, adding 18 new wind measurements, also finding generally close agreement with the Voyager wind profile, except for features associated with a northern great dark spot. They also obtained winds from archived HST observations from June (9 vectors) and November of 1994 (14 vectors) and September 1995 (8 vectors). About half of the November vectors deviated by large amounts from the Voyager profile, moving as companions to what is thought to be an unseen vortex, perhaps formerly associated with a dark spot. The south polar dark band, with a wavenumber-1 latitudinal variation, was seen in these Hubble images, as it was in Voyager images.

An additional 19 wind measurements were obtained by Sromovsky et al. (2001b) from 1998 HST images. These were mostly consistent with the Voyager wind profile, again with exceptions related to bright companion clouds. They also combined 1995, 1996 and 1998 observations to determine new zonal and vorticity profiles, obtained by fitting densely sampled latitudinal regions with special functions. A special effort to track dark spots and associated companion clouds by Sromovsky et al. (2002) provided a few very accurate long-term drift rates, and evidence for sinusoidal and non-sinusoidal variations, and for companion clouds at latitudes substantially displaced from the associated vortex. Similar efforts have been made recently analyzing multi-year and multi-telescope data showing a new dark spot and associated bright companion (Hueso et al., 2017b).

Keck AO imaging at near-IR wavelengths provided very detailed views of Neptune's cloud features, but only a limited amount of published wind data has resulted. The most accurate results seem to be those of Fry and Sromovsky (2004), based on three two-night Keck II/NIRC2 imaging runs from August 2003 and July and August 2004. Images from August 2003 are shown in Fig. 4.25 in linear and logarithmic enhancements to show both high- and low-contrast cloud features. Fry and Sromovsky (2004) tracked a total of 212 cloud features, 160 with uncertainties less than 80 m s^{-1} and 37 with errors less than 20 m s^{-1}. Binning and averaging results in 2.5° latitude bins (plotted as red points in Fig. 4.24) resulted in remarkably good agreement with the Voyager profile from 40° S to 72° S, but considerable dispersion away from that profile was seen at other latitudes, where it seemed that the Voyager profile was an upper bound to the wind measurements. This might be due to wave interactions that produced features that did not follow the local zonal flow. Even more dispersion was found in results of Martin et al. (2012), based on 2001 Keck II AO observations with the NIRSPEC imager, but because individual measurements with estimated errors were not published, it is difficult to incorporate these results into a more comprehensive analysis. They also found what appear to be periodic variations in wind speed that were not seen in any prior cloud tracking work, including the detailed Voyager analysis that is based on data of much higher spatial resolution, and thus these variations might well be due to some artifact. A significant dispersion of Neptune's zonal winds was also found from an analysis of July 14 and 16, 2009 Keck AO images by Fitzpatrick et al. (2014), but was limited to tracking time spans of a few hours or less. This study provided a more detailed error analysis and a generally smaller dispersion

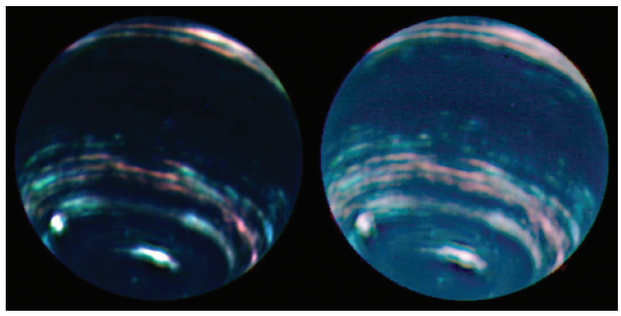

Figure 4.25 Keck II/NIRC2 near-IR color composites using J (1.26 μm), H (1.62 μm) and K′ (2.3 μm) images for R, G and B components respectively. A linear enhancement is shown on the left and a log enhancement on the right. Pink clouds are high and optically thin; white clouds, high and optically thick. Credit: W. M. Keck Observatory.

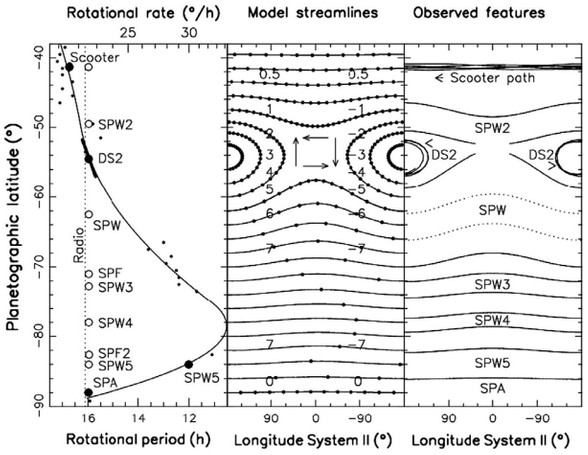

Figure 4.26 Rotational period, streamlines and observed features around Neptune's south pole. From Karkoschka (2011). In this model, jets are not purely zonal, but follow a meandering sinusoidal path around Neptune.

relative to Voyager results, especially for winds measured in the K′ spectral band, which senses higher-altitude features than those measured in the H band. More Keck observations would certainly help to understand these deviations.

Interesting new results have been derived from a comprehensive analysis due to Karkoschka (2011). He used Voyager and Hubble observations of Neptune's South Polar Wave and South Polar Feature to establish a baseline of ∼20 years, arguing that their rotational period over that interval (15.9663±0.0002) is the true interior rotation period of Neptune instead of the radio period of 16.108±0.006 (Lecacheux et al., 1993). He also presented a picture of zonal flow along stationary streamlines that followed wavenumber-1 latitudinal variations, generating meridional wind speeds modeled as $v(\lambda, \phi) = v_{\max}(\phi) \times \sin(\lambda)$, with $v_{\max}(\phi)$ peaking at 7 m s^{-1} between 67° S and 82° S. This picture of stationary (in Karkoschka's System II frame) streamlines, and mass flow that follows them in a wavenumber-1 meander of amplitude that varies with latitude, achieves a very good consistency with the oscillations found by Sromovsky et al. (1993) of the DS2 and "Scooter" (a bright cloud near 42° S), for which there has been no viable alternative explanation. Karkoschka also found and tracked high-latitude features that filled in missing information at 89° S and 86° S, and an asymmetry that was used to define a period for 82°–86° S. These high-latitude data points seem to rule out the possibility of near-polar solid-body rotation at an angular rate of several ° hr^{-1} relative to the interior, as seems to be present on Uranus.

Information about the vertical wind shear has been inferred most directly from 1985, 1988 and 1989 stellar occultations of Neptune (French et al., 1998), which are in good agreement with each other and with vertical wind shear inferred by Conrath et al. (1989) from horizontal temperature gradients measured by IRIS (and the thermal wind equation).

4.12.2 Altitudes of Neptune's Clouds

The effective pressure at which Neptune's discrete cloud features occur are generally much lower than those of Uranus, with many cloud features apparent in near-IR K′ images, while Uranus images in that filter rarely show any discrete clouds. However, the effective pressures do vary considerably from cloud to cloud. Sromovsky et al. (2001a) found altitudes of 60±20 mbar for the brightest northern cloud feature, 230±40 mbar for a large bright feature near 45° S, and 190±40 mbar for a smaller and dimmer feature near 30° S. Roe et al. (2001) obtained 84±26 mbar for a northern cloud and 140^{+50}_{-30} mbar for a southern feature. Gibbard et al. (2003) found effective pressures of 20–45 mbar for features between 30° N and 45° N, and 100–270 mbar for southern features between 30° S and 50° S. These are in general agreement that northern cloud features are found at higher altitudes than southern features, and also in agreement that all of the discrete clouds extend well above the methane condensation level near 1.4 bar, but rarely get above the tropopause level near 100 mbar. These clouds are likely formed of methane ice. Two-wavelength color composite images of Neptune make it clear that clouds of different altitudes are also present at the same latitudes. The level to which Neptune's wind measurements refer are thus somewhat uncertain, but likely average somewhere between 100 and 200 mbar. The vertical wind shear in this region at low latitudes can reach 30 m s^{-1} per scale height. The scale height in this region is about 22 km, and the altitude difference between 100 and 200 mbar is about 15 km. Thus, at low latitudes, where wind speeds reach up to 400 m s^{-1}, the vertical wind shear might contribute a variation up ∼10% from the measured mean.

4.13 URANUS AND NEPTUNE: EFFECTS OF LATITUDINAL VARIATIONS IN METHANE MIXING RATIOS

In 2002, using observations with the Space Telescope Imaging Spectrograph (STIS), which included the key spectral region from 815 nm to 835 nm where methane and hydrogen absorptions have comparable but different spectral absorption signatures, Sromovsky et al. (2014) showed that the north polar region of Uranus was depleted in methane by amounts comparable to those inferred for the south polar region by Karkoschka and Tomasko (2009) and Sromovsky et al. (2011) from 2002 STIS observations. An approximate variation with latitude is shown in Fig. 4.27. This is derived assuming that the variation in methane mixing ratio has the same vertical variation as at the equator, except for a scale factor, and is parameterized by the deep mixing ratio inferred from the scale factor variation. The actual variation appears to be concentrated in the upper troposphere. With the deep mixing ratio assumed constant at the equatorial value, the latitudinal variation appears to be limited to pressures less than approximately 3–4 bar (Sromovsky et al., 2014). A similar latitudinal variation of the effective methane mixing ratio was observed on Neptune (Karkoschka and Tomasko, 2011), although high northern latitudes were not accessible to measurement and thus its north–south symmetry can only be surmised by analogy with Uranus. The pattern inferred from STIS observations is suggestive of a downwelling of atmospheric motions near the polar regions and upwelling at low latitudes. Microwave observations (de Pater et al., 1989; Hofstadter et al., 2007) seem to prefer polar downwellings

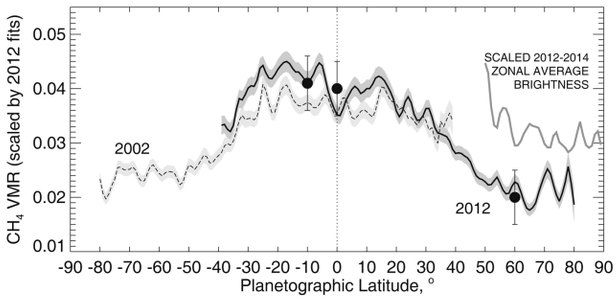

Figure 4.27 Latitudinal variation in the effective upper tropospheric mixing ratio derived from analysis of 2002 and 2012 STIS spectra. The relative variation is scaled by absolute determinations using full radiative transfer model results (plotted as filled circles). From Sromovsky et al. (2014).

reaching much greater depths than indicated by STIS results, and a recent multi-wavelength study of Neptune (de Pater et al., 2014) suggests rising motions at mid-latitudes and downwelling at both equator and polar regions, as suggested by earlier analysis of Voyager thermal spectra (Flasar et al., 1987). In any case, the methane mixing ratio cannot be expected to be independent of latitude. In the following we consider one implication of such a variation on dynamics.

Although methane is a minor constituent (2–4% in volume mixing ratio) of the atmospheres of Uranus and Neptune, its molecular weight is so large that variations of the mixing ratio with latitude can have a significant influence on the zonal wind, depending on the depth to which the latitudinal gradients extend. A latitudinal gradient in atmospheric density on isobars implies a vertical wind shear satisfying the relation (Sun et al., 1991)

$$\partial u_g/\partial p = \frac{1}{f}\frac{\partial}{\partial y}\left(\frac{1}{\rho}\right), \tag{4.9}$$

where u_g is the geostrophic zonal wind speed, p is pressure, f is the Coriolis parameter, ρ is density and y is the distance along an isobar in the direction of increasing latitude. This expression is a shallow atmosphere approximation. A more general expression can be found in Pedlosky (1987a).

Since density variations can be produced by temperature or compositional variations, it is useful to separate these two effects. The following approximate separation was given by Sun et al. (1991):

$$\partial u_g/\partial p = \frac{R_d}{fp}(\partial T/\partial y + CT\partial q/\partial y), \tag{4.10}$$

where R_d is the gas constant for dry (methane-free) atmosphere, $C = (1-\epsilon)/\epsilon$, with $\epsilon = m_c/m_d$ and m_c and m_d are molecular weights of dry and condensable gas (CH_4) respectively, $q = \rho_c/\rho_d$ is the mixing ratio of condensable gas, and T is temperature. According to these relationships, if the zonal wind velocity increases with altitude, density must increase with latitude. Conversely, the decrease of density with latitude towards the Uranian poles (due to methane depletion) should produce a negative vertical wind shear.

Uranus' rotational north pole is actually its IAU south pole, so that the density gradient being negative in that direction should make the vertical wind shear negative (i.e. opposite to the direction of planetary rotation) and thus in an eastward direction relative to the IAU coordinate system. This means that if the vertical wind shear acted from a zero value at significant depths (still only a small fraction of the planet's radius), it would integrate to a large eastward wind that would tend to oppose the observed westward jet present in both hemispheres of Uranus.

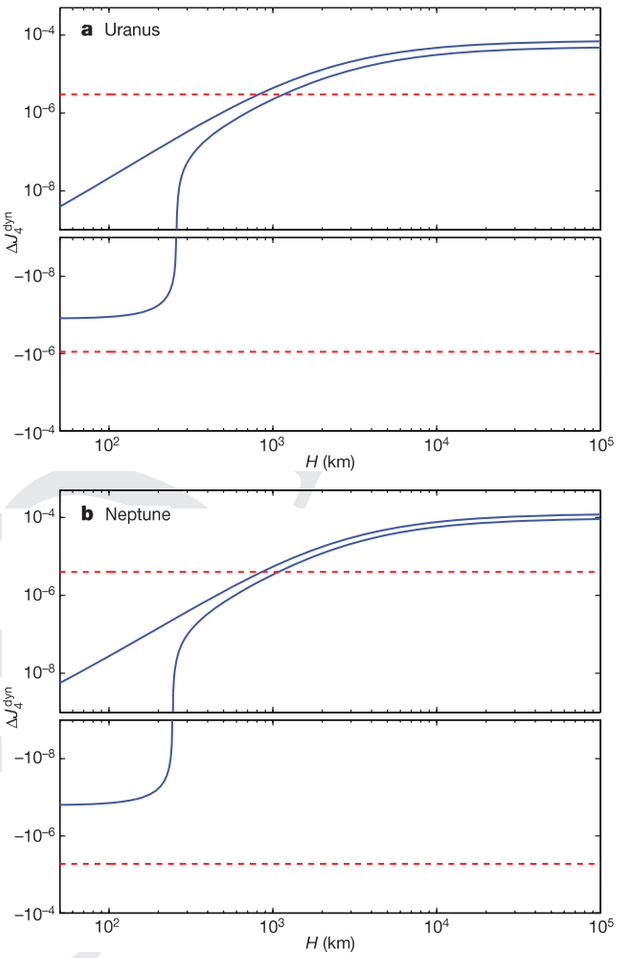

Figure 4.28 The dynamical contribution to J_4 (ΔJ_4^{dyn}) as a function of an e-folding decay height (H) of the zonal winds for (a) Uranus and (b) Neptune. All possible solutions for ΔJ_4^{dyn} using the range of interior models explored by Kaspi et al. (2013) are between the two solid lines for each planet. The dashed lines are the maximum and minimum possible values for ΔJ_4^{dyn}, calculated by the difference between the observed J_4 and J_4^{static} obtained from static interior models. Only solutions between the two dashed lines are possible, so that H must be no more than ~1000 km for both planets. From Kaspi et al. (2013).

4.14 URANUS AND NEPTUNE: GRAVITATIONAL CONSTRAINTS ON THE DEPTH OF ZONAL JETS

How deep the cloud-top winds extend into the depths of the atmosphere is key to understanding their overall dynamics. The existence of the strong jets at the cloud-top level has been

related to shallow atmospheric processes within a few orders of magnitude of the cloud-top pressures on Uranus and Neptune (Read, 1987; Liu and Schneider, 2010; Lian and Showman, 2010), but also to processes that extend very deeply into the interior (e.g., Aurnou et al., 2007). If the zonal jets extended to great depths they would affect the gravity field of the planet, and thus gravity measurements provide a constraint on the depth of the circulation (Hubbard, 1999; Kaspi et al., 2010).

Hubbard et al. (1991) used Voyager measurements of cloud-top winds and of the gravitational harmonics of Neptune to conclude that the differential rotation of Neptune can only involve the outermost few percent of Neptune's mass. More recently, Kaspi et al. (2013) have shown that the measured fourth-order gravity harmonic, J_4, constrains the zonal flow to no more than the outermost 0.15% of the total mass of Uranus and the outermost 0.2% of the total mass of Neptune. Therefore, the dynamics appear to be confined to a thin weather layer no more than about 1000 km deep on both planets, or to within the top few thousand bar rather than the previously estimated top few hundred thousand bar. This analysis was obtained by placing an upper limit on the difference between the observed J_4 and the J_4 contribution of a static planet over a wide range of interior structures, and comparing this difference to the maximal possible contribution to J_4 from dynamics (Fig. 4.28). Placing such constraints for Jupiter and Saturn in a similar method using the known low-order harmonics such as J_4 is impossible, due to the much stronger latitudinal variation of the wind structure on those planets. This therefore requires better determination of the odd- and high-order gravity harmonics, as will be obtained by the Juno and Cassini spacecraft for Jupiter and Saturn respectively in 2017.

4.15 THEORIES AND MODELS FOR ZONAL JETS ON GIANT PLANETS

4.15.1 Jet Structure

Because the giant planets rotate rapidly, the flow at large scales is expected to be geostrophically balanced, implying a Rossby number $\mathrm{Ro} = U/fL \ll 1$, where U is a characteristic wind speed, L is the characteristic flow length scale and $f = 2\Omega \sin\phi$ is the Coriolis parameter. As a result, geostrophic balance is expected to hold on large scales; this implies that, in the horizontal momentum equation, the dominant force balance is between pressure gradient and Coriolis forces. In such a flow, the balance equation for the three-dimensional vorticity reads (e.g. Pedlosky, 1987a, p. 43)

$$2(\mathbf{\Omega}\cdot\nabla)\mathbf{v} - 2\mathbf{\Omega}(\nabla\cdot\mathbf{v}) = -\frac{\nabla\rho\times\nabla p}{\rho^2}, \tag{4.11}$$

where $\mathbf{\Omega}$ is the planetary rotation vector, $\mathbf{v}$ is the three-dimensional velocity vector, ρ is density and p is pressure. Casting this equation in a cylindrical coordinate system centered on the rotation axis yields

$$2\Omega\frac{\partial u}{\partial z_*} = -\frac{\nabla\rho\times\nabla p}{\rho^2}\cdot\hat{\lambda}, \tag{4.12}$$

where Ω is the rotation rate, u is the zonal wind, z_* is the coordinate parallel to the rotation axis and $\hat{\lambda}$ is the unit vector in the zonal (longitudinal) direction. It can be shown that, to a good approximation, this equation is equivalent to (e.g., Kaspi et al., 2009; Showman et al., 2011a)

$$2\Omega\frac{\partial u}{\partial z_*} \approx \frac{g}{\rho}\left(\frac{\partial\rho}{\partial y}\right)_p \tag{4.13}$$

where g is gravity, y is northward distance, and the derivative is taken at constant pressure – see Eqs. (4.9) and (4.10).

Equation (4.13) implies that if the fluid is barotropic – meaning that density does not vary on isobars – then the zonal wind will be constant along coordinate surfaces parallel to the planetary rotation vector. This is similar to the standard Taylor–Proudman theorem (e.g. Pedlosky, 1987a) but is more general, because no assumption of constant density is required; indeed, Eq. (4.13) holds for a barotropic, geostrophically balanced fluid even if the density varies by orders of magnitude across the system (as it does on Jupiter). On the other hand, if density varies on isobars – as is observationally known to occur above the cloud levels on all four giant planets, for example – then the zonal wind will vary along surfaces parallel to the rotation axis. This is similar to the standard shallow-atmosphere thermal-wind equation (e.g. Holton, 2004, p. 70).

Given this framework, early studies suggested two possible scenarios for the structure of the zonal jets on the giant planets. Convective mixing tends to homogenize the entropy, and it is typically assumed that this will lead to deviations from a barotropic state that are small in the interiors of the giant planets. If so, the zonal wind should be relatively constant on surfaces parallel to the rotation axis – Eq. (4.13). In one scenario it is typically assumed that these deep winds are small relative to those measured in the cloud layer, and that the zonal jets die out within several scale heights of the cloud layer (e.g., Hess and Panofsky, 1951; Ingersoll and Cuzzi, 1969). This would require significant variations of density on isobars within and immediately below the cloud level – Eq. (4.13) – which might result from latent heating or radiative effects such as absorption of sunlight or IR cooling to space that differs between belts and zones. Other studies, however, argued that the fast winds observed at the cloud level continued in a nearly barotropic fashion on cylinders through the interior (e.g. Busse, 1976). As emphasized by Vasavada and Showman (2005), hybrid scenarios are also possible where significant thermal wind shear in the stably stratified portion of the atmosphere is superposed on fast, nearly barotropic zonal jets in the interior.

Of course, convective transport of the interior heat flux on giant planets implies that ascending and descending convective plumes have differing temperatures and therefore that the interior is not in a barotropic state. Is is worth asking how strong the deviations from barotropicity will be. This question is currently difficult to address with direct numerical simulations, because three-dimensional models of convection in the interior of the giant planets are overforced, meaning that they adopt heat fluxes much too large, which may lead to density variations much greater than those occurring in the interiors of the giant planets. Motivated by this difficulty, several authors have applied scaling laws to estimate the density variations and hence, via Eq. (4.13), the thermal wind shear in the deep interior. These estimates suggest that, at heat fluxes relevant to the giant planets, the zonal winds in the deep molecular envelope are indeed nearly baro-

tropic, with variation of zonal wind throughout the interior (on surfaces parallel to $\mathbf{\Omega}$) that are small compared to the typical amplitude of wind observed in the cloud layer (Liu et al., 2008; Showman and Polvani, 2010; Showman et al., 2011b; Showman and Kaspi, 2013). Nevertheless, these scaling arguments remain tentative; careful numerical simulations and extrapolations to the Jovian regime may allow better assessments of the possible amplitudes of wind shear in the interior.

4.15.2 Mechanisms for Driving the Jets

Vasavada and Showman (2005) provided a detailed review of theories and models for driving the jets on the giant planets; here, we recap only the key points and summarize developments over the past eight years or so. Two categories of model have been invoked to explain the jets on the giant planets. In one, dubbed the "shallow forcing" scenario, the jets are driven by baroclinic instabilities, moist convection or other processes in the outermost layers of the planet. These scenarios have typically been investigated with atmospheric models adapted from the terrestrial geophysical fluid dynamics (GFD) community. In another, dubbed the "deep forcing" scenario, convection throughout the molecular envelope (a layer $\sim 10^4$ km thick) drives differential rotation in the interior, which manifests as jets at cloud level. These scenarios have been investigated with Boussinesq and anelastic convection models that share significant heritage with models used by the geodynamo community.

Observations on Jupiter and Saturn indicate that eddies at the cloud level transport momentum into the cores of the zonal jets (Salyk et al., 2006; Del Genio et al., 2007; Del Genio and Barbara, 2012) – see Section 4.8. The amplitude of this forcing is sufficiently large that the eddies must be atmospheric in nature, i.e., the amplitudes of $\overline{u'v'}$ associated with these eddies cannot extend more than a few bar into the interior. Thus, shallow, cloud-level forcing is strongly implicated in driving the jets. Eddy momentum fluxes in the deep interior could also contribute, but observations are not yet able to assess this issue.

It is important to emphasize that the issue of shallow or deep *forcing* of the jets is distinct from the issue of shallow or deep *structure* of the jets (Vasavada and Showman, 2005; Showman et al., 2006). Even if the eddy accelerations that drive the jets are localized to the atmosphere, the jets themselves could potentially extend deep into the interior (Showman et al., 2006; Lian and Showman, 2008). On the other hand, some recent models of convection in the deep interior suggest that the jets may be strongest toward the outer layers of the planet (e.g. Kaspi et al., 2009). A related point is that the issue of deep versus shallow forcing, as defined above, is not equivalent to the issue of whether the jets are driven by "solar heat" or "internal heat." For example, moist convection is a fundamentally atmospheric process; condensation of water occurs at pressures of ~6–8 bar on Jupiter, and models of this process suggest that it generates momentum fluxes localized to the upper troposphere (Lian and Showman, 2010). However, most sunlight is absorbed at pressures less than several bar (Pérez-Hoyos and Sánchez-Lavega, 2006b), so the heat flux transported by moist convection – despite its shallow nature – is primarily linked to the interior heat flux. Dietrich et al. (2017) have recently studied the effects of thermal gradients and thermal winds in the upper layer with geostrophic zonal flows.

4.15.3 Jets from Shallow-Layer Forcing

Atmospheric jet formation scenarios generally assume that the jets result from the interaction of large-scale atmospheric turbulence with the β effect arising from the gradient in the Coriolis parameter with latitude. A hierarchy of models have been explored. One-layer systems that have been applied to the giant planets include the horizontally nondivergent two-dimensional model, the one-layer quasi-geostrophic (QG) model and the shallow-water model. Most of the three-dimensional investigations have adopted the primitive equations, although a few multi-layer QG investigations of giant planet atmospheres have also been carried out.

In one-layer models, the turbulence that drives the flow and organizes into jets must be injected by hand; this is typically performed by introducing small-scale sources of vorticity to parameterize the effect of convection or baroclinic instabilities on the cloud-layer flow. Under the rapidly rotating conditions appropriate to the giant planets, such models typically show that multiple zonal jets and vortices can form from small-scale forcing (see Vasavada and Showman, 2005, for a review). Typically, the meridional jet width is close to the Rhines scale, $(U/\beta)^{1/2}$. Most work to date has been done using the two-dimensional, horizontally nondivergent model (Fig. 4.7). This system provides the simplest and cleanest environment in which to understand the interaction of atmospheric turbulence with the β effect, but it ignores buoyancy effects, lacks gravity waves and exhibits a Rossby deformation radius that is infinite (in contrast to Jupiter and Saturn, where the deformation is a few percent of the planetary radius). While numerical simulations with such models can generate zonal jets, these jets do not exhibit the equatorial intensification of the jet speed that occurs on Jupiter and Saturn (e.g., Nozawa and Yoden, 1997; Huang and Robinson, 1998, and many others). When strong jets are present, such models typically also do not reproduce the rich array of stable, long-lived vortices occurring on Jupiter. This may result from the absence of a deformation radius in this system. This class of model is best viewed as a process model of jet formation in a simple environment rather than realistic circulation models of Jupiter and Saturn.

One-layer shallow-water models provide a more realistic representation by including buoyancy effects (in the form of a spatially variable layer thickness), which allows the existence of gravity waves and other buoyancy-related effects while still ignoring the details of atmospheric vertical structure. The deformation radius is finite, and thus this model and the related one-layer QG model are the simplest models that can explore the effects of the deformation radius on the atmospheric flow. At present there are only a few forced–dissipative studies of jet formation on the giant planets using the shallow-water equations. Showman (2007) forced the flow by introducing localized mass sources, intended to represent the mass transport by moist convection (i.e., thunderstorms) into the upper troposphere. Scott and Polvani (2007) introduced a more globally continuous forcing in an otherwise similar study. Both investigations showed that multiple zonal jets like those on the giant planets

can result from the small-scale forcing. Li et al. (2006) used a one-layer QG study, adopted localized forcing and likewise showed the emergence of multiple zonal jets. Unlike most two-dimensional nondivergent investigations, Jovian-like vortices occur naturally in these shallow-water flows. Extending earlier theoretical work in the QG system, Okuno and Masuda (2003) and Smith (2004) showed how zonal jets can be suppressed when the deformation radius is sufficiently small, leading to a flow dominated by vortices instead.

Interestingly, unlike the two-dimensional nondivergent system, forced–dissipative shallow-water turbulence naturally produces an intensification of the jet speed at the equator relative to mid-latitudes. Under Jovian conditions (Ro $\sim$ 0.01 and deformation radii a few percent of the planetary radius), most shallow-water studies produce a westward equatorial jet (Cho and Polvani, 1996a; Iacono et al., 1999; Showman, 2007; Scott and Polvani, 2007). This may provide a reasonable description of the dynamics on Uranus and Neptune, but is inconsistent with the equatorial superrotating jets on Jupiter and Saturn. More recently, however, Scott and Polvani (2008) presented shallow-water simulations demonstrating the emergence of a strong eastward equatorial jet from small-scale forcing and large-scale damping under Jovian conditions. They argued that the defining ingredient allowing the eastward jet in their model is the use of radiative rather than frictional damping, but this is inconsistent with the results of Showman (2007), who found westward equatorial jets in models that were radiatively damped. It seems likely that particular combinations of both forcing and damping are necessary. However, the specific dynamical mechanism that allows the emergence of the eastward equatorial jet in the Scott and Polvani (2008) model remains to be identified, and it is not clear from their model why one would expect eastward equatorial flow on Jupiter and Saturn but westward equatorial flow on Uranus and Neptune. Future work would be useful to clarify the mechanisms controlling the equatorial jet in the shallow-water system and to assess its relevance to the equatorial jets on the four giant planets.

The stability of the zonal jets is an intriguing topic that remains incompletely understood. At most latitudes, the observed zonal jet patterns on Jupiter and Saturn have remained remarkably constant in time, exhibiting little change in the speed or latitudes of the jets between the Voyager flyby and Cassini observations (Fig. 4.13). The main exception is Saturn's broad equatorial jet, which seems to have exhibited a slowdown between the Voyager and Cassini eras, although a few of the Jupiter and Saturn off-equatorial jets have also exhibited modest changes. This overall constancy of the zonal jets on decadal timescales argues that the jets are dynamically stable or perhaps close to neutral. In this regard, a puzzling observation is that, at certain latitudes, the zonal-mean value of $\beta - U_{yy}$ changes sign on both Jupiter and Saturn, implying that the jets violate the barotropic stability criterion. Calculation of Ertel's potential vorticity is more difficult because it requires knowledge of thermal structure in addition to vorticity. Nevertheless, recent data analyses by Read et al. (2009) show that the meridional gradient in zonal-mean PV seems to exhibit sign changes at several latitudes, implying that the jets violate the Charney–Stern stability criterion for baroclinic instability as well. Technically, since these are only necessary (but not sufficient) conditions for instability, violation of these stability criteria does not imply that the fluid is unstable, but rather simply that the stability criterion provides no information. Nevertheless, numerical simulations of atmospheric turbulence using two-dimensional and shallow-water models generally produce jet profiles that are stable against these criteria, which suggests that the violation of the criteria on Jupiter and Saturn is a real issue that needs explaining.

Dowling (1993, 1995a,b, 2014) and Read et al. (2009) argued that Jupiter and Saturn are close to neutrally stable with respect to another stability criterion due to Arnol'd, despite the observed sign reversals in the meridional PV gradient. One way that a flow can be stable in the presence of sign reversals of the PV gradient is if the zonal jets are underlain by a nonzero zonal flow in the deeper troposphere. In the context of a 1.5-layer shallow-water model, this would be equivalent to assuming that the abyssal layer contains nonzero zonal jets, which then influence the stability properties of the overlying weather layer. Indeed, if the jets in the weather layer are neutral to Arnol'd's second stability criterion, it is possible to infer the structure of the jets in the underlying abyssal layer from the observed jet properties, given information (or plausible assumptions) about the vertical stratification (Dowling, 1993, 1995a). Thus, these stability-criterion arguments provide tentative evidence that the off-equatorial zonal jets (to which Arnol'd's stability theorems apply best) extend at least some considerable distance into Jupiter's interior. Nevertheless, these 1.5-layer stability arguments have yet to address the question of whether or how the required abyssal-layer jets are stable; thus, rather than solving the stability puzzle, these investigations are essentially shifting the puzzle one layer deeper into the atmosphere. Lian and Showman (2008) presented three-dimensional turbulent models of tropospheric dynamics in which the jets tend toward neutrality with respect to Arnol'd's second stability criterion, including in some cases reversals in the sign of the PV gradient. This is encouraging, but more work is needed in this area.

Ingersoll and Pollard (1982) suggested a modified stability criterion due to the interior dynamics being controlled by convectively driven columns which have effectively an opposite beta effect (due to columns being stretched as they move poleward, rather than squeezed in a thin atmosphere). They derive a modified stability criteriion where $-3\beta - U_{yy}$ becomes the condition for barotropic instability, and indeed the jets on Jupiter and Saturn do not violate this stability criterion. Using a two-layer model with a deep abyssal layer with such a negative beta effect, Kaspi and Flierl (2007) showed that under such configuration, multiple stable, baroclinicllly driven, jets emerge; as on the real planets, these jets violate the condition that $U_{yy} - \beta$ does not change sign, but are stable in reference to the Ingersoll and Pollard (1982) stability criterion.

Three-dimensional models have the advantage that they allow vortex stretching and baroclinic effects that can play a major role in determining the properties of macroturbulence and the jet structure. The injection scale of baroclinic instability, for example, is proportional to the Rossby deformation radius (Eady, 1949; Rhines, 1979; Salmon, 1978; Merlis and Schneider, 2009). If energy is halted at the Rhines scale, then the scale separation between the Rhines scale and the Rossby deforma-

tion radius, which follows the QG supercriticality (Held and Larichev, 1996), can imply the importance of inverse energy cascade and eddy–eddy interactions in the atmosphere (Jansen and Ferrari, 2012; Chemke and Kaspi, 2015a). Both analysis of Jupiter observations (Theiss, 2006) and three-dimensional numerical simulations of Jupiter (Sayanagi et al., 2008) suggest that the latitude where supercriticality equals one plays an important role in determining turbulence isotropy: regions where supercriticality is larger than one will be more isotropic and dominated by vortices, while equatorward regions where supercriticality is less than one are dominated by jets. Chemke and Kaspi (2015a) found that poleward (equatorward) of the latitude where supercriticality equals one, eddy–eddy (eddy–mean) interactions are most dominant in maintaining the jets. Yet, despite the apparent importance of eddy–eddy interactions in the process of jet formation, Chemke and Kaspi (2015a) showed that even in three-dimensional simulations where eddy–eddy interactions are omitted, Rhines scale multiple jets form and can reach to high latitudes where their stability is maintained by eddy–mean interactions.

Significant advances have been made over the past few years on fully three-dimensional atmospheric models of Jovian dynamics. Following on from early work by Williams (2003b) and others, Lian and Showman (2008) presented three-dimensional primitive equation models showing that baroclinic instabilities in the cloud layer – driven by meridional temperature contrasts associated with the latitudinal insolation gradient and/or belt-zone temperature variations – can generate multiple zonal jets, and that these jets can penetrate far below the level of the forcing. The statistical distribution of eddy accelerations (e.g., the distributions of $u'v'$) in their model exhibits a strong resemblance to the distributions of $u'v'$ measured on Jupiter and Saturn. Like the jets on Jupiter and Saturn, the Lian and Showman (2008) models exhibited profiles of zonal-mean potential vorticity that violate the Charney–Stern stability criterion and trend toward neutrality with respect to Arnol'd's second stability criterion (Dowling, 1995b). Moreover, when sharp meridional temperature gradients are introduced near the equator, equatorial superrotation emerged, consistent with earlier results by Williams (2003b).

Several global atmospheric models have now been published that explain the overall features of the atmospheric circulation on all four giant planets, including multiple zonal jets in the mid-to-high latitudes of Jupiter and Saturn, the three-jet patterns on Uranus and Neptune, the existence of equatorial superrotation on Jupiter and Saturn, and the existence of equatorial subrotation on Uranus and Neptune. Lian and Showman (2010) introduced a hydrological cycle to test the idea that large-scale latent heating plays a crucial role in the cloud-level circulation (e.g. Ingersoll et al., 2000). Figure 4.29 shows an example of their results. In addition to explaining the overall circulation patterns of all four planets and the transition in equatorial jet direction between Jupiter/Saturn on the one hand and Uranus/Neptune on the other, the Jupiter and Saturn models by Lian and Showman (2010) produce localized "storm" features that bear a strong qualitative similarity to moist-convective storm events observed on Jupiter and Saturn (see Section 4.5). Schneider and Liu (2009) presented dry primitive-equation models for Jupiter, forced by a meridional

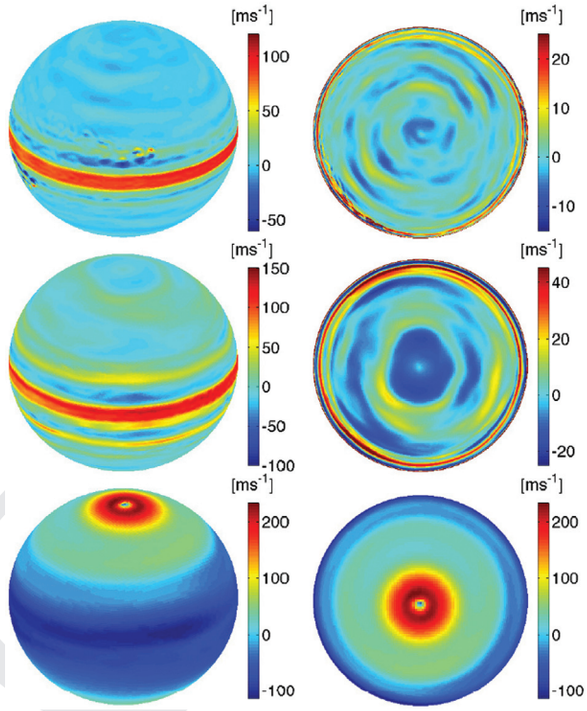

Figure 4.29 Atmospheric flow on the giant planets in three-dimensional circulation models from Lian and Showman (2010). The globes depict the zonal wind (given in scale bars in m s^{-1}) for simulations of Jupiter (top row), Saturn (middle row) and a case representing Uranus and Neptune (bottom row). The left column shows an oblique view and the right column shows the view looking down over the north pole. In these models, the circulation is driven by large-scale latent heating associated with condensation of water, which is assumed to be 3, 5 and 30 times solar in the Jupiter, Saturn and Uranus/Neptune models, respectively. Consistent with observations, numerous zonal jets including equatorial superrotation emerge in the Jupiter and Saturn models, while a broad jet pattern including equatorial westward flow and high-latitude eastward flow emerges on Uranus and Neptune. These are the first models to self-consistently capture the dichotomy in equatorial jet direction between Jupiter/Saturn on the one hand and Uranus/Neptune on the other in the context of a single model.

solar-heating gradient and by a simple dry-convective parameterization, that show the emergence of equatorial superrotation and multiple off-equatorial jets under Jovian conditions. Liu and Schneider (2010) subsequently extended this model to all four giant planets; this, like Lian and Showman (2010), shows a transition from equatorial superrotation on Jupiter and Saturn to equatorial subrotation on Uranus and Neptune. Taken together, these models are major successes and show how atmospheric turbulence can explain observations at the cloud levels of the giant planets. Nevertheless, some details, such as the existence and locations of major vortices like the Great Red Spot and the details of the zonal jet profiles versus latitude, were not reproduced, so additional work will clearly be useful.

4.15.4 Jets from Deep Forcing

Around the same time as when the mechanisms for jet formation on giant planets by shallow geostrophic turbulence

emerged (e.g., Rhines, 1975, 1979; Williams, 1978, 1979), a completely alternative approach suggesting that the observed jets are a surface manifestation of concentric cylinders parallel to the axis of rotation also emerged (Busse, 1976, 1994). These theories were based on the fact that if the interior convection homogenizes entropy gradients, then the interior may be nearly barotropic (the right-hand term in Eq. (4.13) is zero), thus allowing the formation of Taylor columns in the interior. The nonlinear interaction of these convectively driven columns has been shown to generate equatorial superrotation and possibly high-latitude jets. The theories discussing this mechanism are summarized in a review by Busse (2002) and are discussed in detail by Vasavada and Showman (2005).

Models of jets formed by interior convection generally investigate the idea that convectively generated Reynolds stresses in the molecular envelopes of the giant planets can cause large-scale, organized differential rotation within the interior, which manifests at atmospheric level as multiple zonal jets. Throughout the 1970s and 1980s, advances were confined mostly to analytic studies, laboratory experiments and numerical simulations in the linear or weakly nonlinear regime. Only over the past ∼15 years have computational resources been sufficient to explore fully three-dimensional convection in rotating spherical shells under strongly nonlinear conditions relevant to the giant planets. Most such models to date have been Boussinesq models that adopt a constant basic-state density and an incompressibility continuity equation, $\nabla \cdot \mathbf{v} = 0$. Over the past five years, however, several authors have investigated anelastic models, which allow the basic-state density to vary radially and adopt a continuity equation $\nabla \cdot (\bar{\rho}\mathbf{v})$, where $\bar{\rho}$ is the specified basic-state density that is a function of radius. Both classes of model filter acoustic waves from the dynamics, which is reasonable under Jovian conditions.

Published Boussinesq models of convection in rotating spherical shells applicable to the giant planets are generally performed with constant-temperature boundary conditions (hot at the inner boundary, cold at the outer boundary) and also assume that the thermal expansivity and other fluid properties are constant with radius. When the Rayleigh number (vigor convection) is sufficiently large and the Ekman number is sufficiently small, these models produce strong zonal flow with speeds that significantly exceed the convective velocities. When carried out in spherical geometry, the equatorial surface flow is eastward in these models, consistent with Jupiter and Saturn but inconsistent with Uranus and Neptune. Early models adopted a thick shell, with an inner to outer radius ratio of 0.7 or less (e.g., Christensen, 2001, 2002; Aurnou and Olson, 2001). These thick-shell models generally produce only a few zonal jets with an equatorial jet that is much wider than those on Jupiter and Saturn. The equatorial jet width in these models is directly controlled by the shell thickness; at the equator, the zonal-wind speed varies smoothly from a peak eastward speed at the outer boundary to a peak westward speed at the inner boundary, which means that the latitude of the westward jet closest to the equator is equal to the latitude at which the so-called "tangent cylinder" outcrops at the surface.

Motivated by this, Heimpel et al. (2005) and Heimpel and Aurnou (2007) showed that, if the shell is thin (with an inner to outer radius ratio of ∼0.9), then the equatorial jet width is

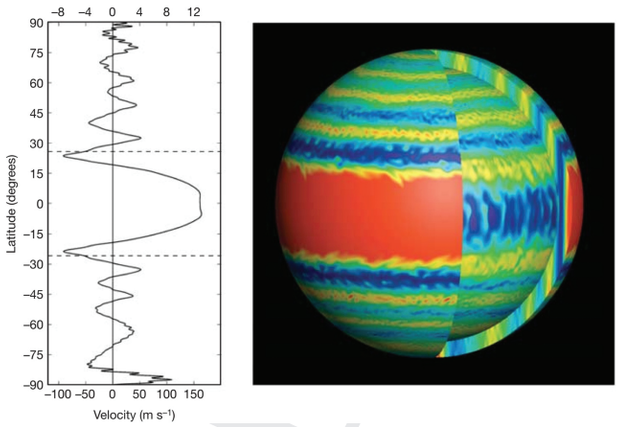

Figure 4.30 Zonal winds in a three-dimensional model of convection in a thin spherical shell from Heimpel et al. (2005). The ratio of the inner and outer radii in the model is 0.9. The model is Boussinesq and thus ignores the increase of mean density with depth that occurs on the giant planets. Equatorial superrotation and multiple off-equatorial jets emerge, qualitatively similar to those on Jupiter.

comparable to those on Jupiter and Saturn, and the flow inside of the tangent cylinder organizes into multiple zonal jets. The similarity of these zonal-flow profiles to those on Jupiter and Saturn is a major success (see Fig. 4.30). Still, the fact that the flow behavior is so strongly controlled by the lower boundary – a boundary that does not exist on Jupiter and Saturn – raises some questions about the extent to which these exquisite results carry over to Jupiter and Saturn themselves. These models also naturally produce a greater heat flux at the poles than at low latitudes, which may help explain the near constancy of the total (solar + interior) heat flux with latitude on Jupiter and Saturn (Aurnou et al., 2008).

On Jupiter and Saturn, the mean density varies by more than four orders of magnitude from the 1 bar level to the deep interior, and this density variation almost certainly will exert important effects on the dynamics. Recently, several anelastic models have been published that incorporate radial density variations and explore their role in controlling the jet properties. These models started with two-dimensional models in the equatorial plane, whose goal is to understand how the compressibility helps control the emergence of differential rotation (Evonuk and Glatzmaier, 2004, 2006, 2007; Glatzmaier et al., 2009) These studies have suggested a mechanism for differential rotation where local generation of vorticity is produced by the expansion of convectively rising fluid and contraction of sinking fluid. Conservation of potential vorticity governs the rate at which vorticity is produced as fluid rises and sinks in the stratified density field.

Kaspi (2008) developed the first three-dimensional anelastic general circulation model for giant planets. The model, based on the nonhydrostatic MITgcm, accounts for the full four-order-of-magnitude variation in density in the interior of giant planets, and uses a realistic equation of state designed for hydrogen–helium high-pressure interiors (Saumon et al., 1995). They have found that, as in the Boussinesq case, conservation of angular momentum constrains the flow to be only along cylinders concentric to the axis of rotation; however, in the anelastic case, this

azimuthal flow develops shear along the direction of the spin axis. This shear is due to the fact that entropy gradients generated by the internal convection drive the system away from a barotropic state resulting in baroclinic shear, Eq. (4.13) becoming

$$2\Omega \cdot \nabla u = \alpha_s \nabla s' \times g, \tag{4.14}$$

where s' are the entropy perturbations from an adiabatic state, and $\alpha_s = \frac{1}{\bar{\rho}} \left(\frac{\partial \rho}{\partial s}\right)_p$ is the entropy expansion coefficient along isobars (Kaspi et al., 2009). Since this expansion coefficient varies significantly with depth, so does the rate of the shear along the direction of the spin axis. Anelastic models using ideal gas equations of state in which such an expansion coefficient is constant have shown only weak shear in the interior (e.g., Jones et al., 2009; Gastine and Wicht, 2012; Cai and Chan, 2012).

All three-dimensional anelastic GCMs exhibit superrotation at the equator, similar to the Boussinesq models. The mechanism involves Reynolds stress convergences, that is, convergences of eddy momentum fluxes in the meridional plane, as a result of correlations between the zonal velocity and the radial and/or meridional velocity component. In this sense, the process for developing superrotation in three-dimensional convective models is analogous to that occurring in stratified shallow-atmosphere models (although the specific physical mechanism for inducing the velocity correlation differs between the cases). Here, in the three-dimensional case, convection columns which form parallel to the direction of the spin axis are tilted eastward and outward (Fig. 4.31) due to refraction by the background planetary vorticity (Kaspi, 2008). This tilt leads to a positive correlation between the zonal eddy velocity and the velocity component in the direction toward or away from the rotation axis (Showman et al., 2011b). This is analogous to the zonal/meridional velocity correlations that occur in a two-dimensional flow on the surface of a sphere (caused in that case, for example, by generation, meridional propagation and breaking of Rossby waves; see, e.g., Vallis, 2006, Section 12.1). In both cases, meridional and/or radial momentum convergence and the formation of zonal jets results.

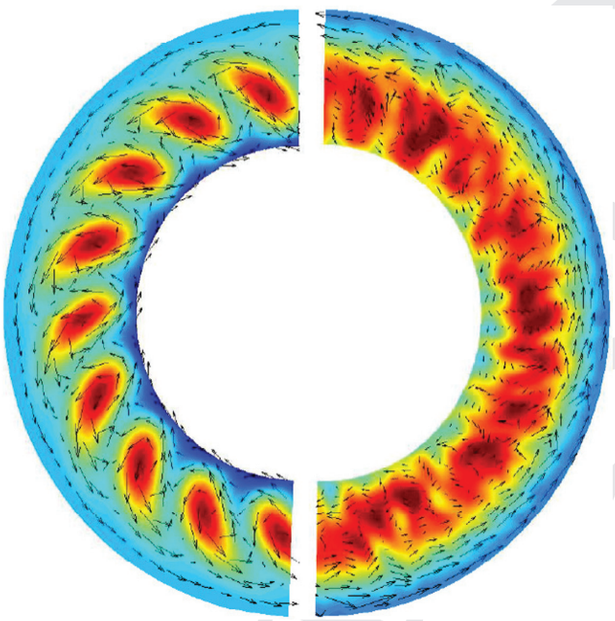

Figure 4.31 Snapshots in the equatorial plane of two anelastic, three-dimensional simulations illustrating how the correlation between the convective velocity components depends on the supercriticality (from Showman et al., 2011b, Fig. 5). Each slice shows half of the equatorial plane of one simulation (note, however, that the simulations each span 360° of longitude). Color depicts streamfunction, and the arrows denote the velocity component in the equatorial plane. The left simulation is weakly supercritical; the strong correlation between outward and eastward velocity components is obvious. The right simulation is strongly supercritical; the correlation between the outward and eastward velocity components is weaker because of the complex, turbulent convective structure. In both cases the momentum flux convergence leads to equatorial superrotation.

Anelastic simulations that are relatively shallow show similar behavior to the Boussinesq simulations where the depth of the lower boundary controls the latitudinal extent of the superrotation region. However, anelastic simulations with a deeper bottom boundary (i.e., an inner to outer radius ratio that is significantly less than 1) have shown that the location of this region of eddy momentum flux convergence and superrotation is almost invariant to the location of the bottom boundary, but rather is a property related to the stratification of the fluid (Kaspi, 2008; Cai and Chan, 2012). Thus, in the anelastic simulations the convective columns form at a characteristic depth which then controls the region of eddy momentum flux convergence and superrotation.

Several studies have explored the transition between the rotationally dominated regime (exhibiting Taylor columns equatorial superrotation) and a buoyancy-dominated regime (generally lacking equatorial superrotation). Aurnou et al. (2007) suggested that this transition is what separates Jupiter and Saturn from Uranus and Neptune, where the latter are in the buoyancy-driven regime where convection columns parallel to the axis of rotation do not form and therefore equatorial superrotation does not occur. However, Uranus and Neptune are both rapidly rotating planets (~17 and ~16 hr, respectively), where on Uranus the interior heat flux is very weak and on Neptune it is almost twice as large as the total solar heat flux. Therefore, there seems to be no simple reason why Uranus and Neptune would be in a regime different from that of Jupiter and Saturn. Kaspi et al. (2009) presented a series of experiments where the ratio between the rotational and convective timescale was varied systematically, and showed that for a Jupiter-like planet the transition from a superrotating equator to a subrotating equator will be around a rotation period of 50 hr. Gastine et al. (2013) presented similar simulations showing the transition between the rotational and buoyancy-driven regimes. Heimpel et al. (2016) presented simulations combining deep-seated zonal jets and the formation of vortices in a shallow layer.

A major challenge regarding all internal convection models (both Boussinesq and anelastic) is that in order to simulate turbulent convection at high Rayleigh numbers these models must be over-forced by 5–10 orders of magnitude in order to compensate for the high numerical viscosity required in such simulations. Christensen (2002) attempted to bridge this gap by suggesting a scaling to the real Jupiter regime, but from the Boussinesq model it is difficult to reliably extract the expected

flow velocities in the interior. Using an anelastic model, Showman et al. (2011b) showed that the flow behavior can be divided into three distinct circulation regimes: two are controlled by the balance between the viscosity and thermal forcing of the model; in the third, at sufficiently large heat flux, or at sufficiently small viscosity, the wind speeds become independent of the viscosity and might be representative of the dynamics of the real planets. However, this third regime can now only be barely achieved by numerical simulations. Since simulations with any realistic heat flux will be impossible in the near future, any interpretation of deep models to the planets will require scaling laws to bridge over these regimes. Nonetheless, these models serve as excellent process models to study the behavior of three-dimensional turbulence in giant planet interiors.

4.16 FUTURE RESEARCH

Current and future goals in giant planet research are split into two broad areas. First, there are new observations and associated proposed spacecraft missions; second, the modeling and theoretical work required to understand these and past observations.

4.16.1 Observational Goals

Many aspects of giant planet atmospheres remain poorly understood, particularly the nature and behavior of the atmosphere at depth, below the visible cloud tops. Future observations are based around two approaches: new instrumentation to probe deeper into planetary interiors, and higher-resolution observations at the cloud level and above.

At depth, probably the most important question for the two gas giants is to determine the depth of the jets and whether the jets at cloud level are a shallow "weather layer" phenomenon, reaching down to a few tens of bar, or the intersection between the planet's surface and counterrotating cylindrical columns that extend throughout the whole fluid envelope (Busse, 1976). This question was recently resolved in favor of a shallow weather layer for both Uranus and Neptune (Kaspi et al., 2013). For Jupiter and Saturn it requires more accurate measurements of the gravitational moments or new techniques for probing beneath the cloud deck.

For all four giant planets the deep water abundance is still an open question. Future observations should aim to measure this and the lowest condensation level for all four planets. The water abundance constrains possible energy sources for moist convection and latent heating, which are thought to be responsible for injecting energy into the flow to drive the eddies and jets. The Galileo probe recorded an unexpectedly low water abundance in Jupiter's atmosphere (Niemann et al., 1998), thought to be a result of entering the atmosphere in a 5 μm hot spot (Showman and Dowling, 2000). It is not known whether this is characteristic of the planet as a whole.

At the cloud level, increased observational resolution along with greater temporal and spatial coverage is required to understand several aspects of the dynamics. High-resolution measurements of winds are required for evaluation of the eddy momentum flux and, combined with higher-resolution temperature measurements, the other terms in the Lorenz (1955) energy cycle. These measurements will determine how important baroclinic conversion processes are on the giant planets. A capability is also desired for observing winds at deeper levels to sufficient accuracy to measure barotropic conversions, which can be linked to those measured at the visible cloud levels and potential vorticity profile features retrieved for the upper atmospheres (of Jupiter and Saturn, so far). Dedicated long-term high-resolution continuous monitoring of atmospheric cloud motions will allow the time variability of the eddy momentum flux to be measured, along with other turbulent diagnostics requiring long time-averaging. Available high-resolution datasets for Jupiter exist over a much shorter time period than, say, the radiative timescale, and while Saturn has seen long-timescale observations, instantaneous coverage has not been global. Such high-resolution observations would also be useful for studying atmospheric waves and their role in transporting energy, and wind variability in regions containing large-scale morphological changes such as the 2010–2011 storm on Saturn (Sánchez-Lavega et al., 2011; García-Melendo et al., 2013; Sayanagi et al., 2013); see Fig. 4.9.

Fully three-dimensional wind fields incorporating the stratosphere are desirable. Above the visible cloud deck winds can be estimated using the thermal wind equation, but Doppler imaging would allow winds to be measured directly from the cloud level into the stratosphere.

It is unknown whether cloud tracking techniques that purport to produce instantaneous two-dimensional velocity fields are actually capable of producing information content down to spatial scales and velocity perturbation amplitudes needed to truly characterize the eddy kinetic energy spectrum over a useful range of wavenumbers. Some effort has been made to address these concerns in the context of artificial data produced by numerical models of Saturn (Sayanagi et al., 2010a), but this is ongoing.

Jupiter's poles have recently been imaged at high resolution by the Juno mission (Bolton et al., 2017; Orton et al., 2017), and Cassini has observed rich meteorology at Saturn's poles (Fig. 4.8); a comparison between the polar dynamics of both atmospheres deserves closer attention. The ongoing Juno mission will provide further images of Jupiter's poles, which will allow better understanding of Jupiter's high-latitude dynamics.

Following the 2009 impact on Jupiter (Sánchez-Lavega et al., 2010; Hammel et al., 2010) there has been increasing interest in more systematic surveys of the planet in methane absorption bands where the debris left but an impact can be easily identified and its evolution studied. Such observations are not key for understanding atmospheric dynamics, but are interesting if the impacts left debris that can be used as tracers of stratospheric motions.

Better measurements of the winds of Uranus and Neptune are certainly possible from the ground using large ground-based telescopes with adaptive optics and using near-IR wavelengths in methane absorption bands that provide high contrast for bright cloud features. For Uranus especially, it is also important to use high signal-to-noise methods to reveal low-contrast cloud features in regions of latitude and longitude away from major storm regions, which have been undersampled by prior observations. As Uranus continues to move towards the northern hemi-

sphere's summer solstice, we will be treated to better and better views of the polar circulation of that planet, and the numerous cloud features that have appeared there will greatly facilitate accurate measurements. New measurement should also reveal whether the large high-latitude north–south asymmetry is seasonal or permanent, as large changes should occur in the polar circulation if the former is true. To better define meandering jets, such as appear to exist on Neptune, and better understand the dispersion of wind speeds on Neptune derived from recent ground-based observations, as well as episodic storm systems on Uranus, more time continuity in the observations would be extremely valuable, but the limited access provided by current observatories that can achieve the required high spatial resolution makes this a difficult task.

4.16.2 Launched and Approved Missions

Cassini will end its tour of Saturn with the Grand Finale in September 2017, and Juno has been orbiting Jupiter since 2016 (Bolton, 2010; Bolton et al., 2017). The ESA mission JUICE will orbit Jupiter and Ganymede in 2029 and later.

Juno's primary mission is to determine the internal structure of the planet by measuring Doppler shifts in the X and Ka bands used by the radio experiment. This has allowed measuring Juno's gravity field up to J10, including measurment of nonzero J3, J5, J7 and J9, which indicate north–south asymmetries in the planet's gravity field (Bolton et al., 2017; Folkner et al., 2017; Iess et al., 2018).

This will allow measuring Jupiter's gravity moments up to at least J12, which should help to settle the question of whether Jupiter's zonal jets are deep or shallow (Hubbard, 1999; Kaspi et al., 2010; Kaspi, 2013, 2018). This measurement is based on the idea that if the jets on Jupiter penetrate deep enough, then they should produce a measurable perturbation to the gravity field of the planet. More models connecting the jet structure to the gravity fields are required to build a complete picture of the relations between the wind and the resulting gravity field. Juno will also provide for the first time measurements of the odd harmonics of Jupiter (Kaspi, 2013), which, if they exist, will provide information about north–south asymmetries in the deep wind structure, which should also help in constraining theories for the formation of the jets. Juno will also use microwave sounding to detect thermal radiation from deep below the visible cloud deck (to at least 100 bar, possibly to 1000 bar according to Bolton, 2010, Fig. 2). This will constrain the vertical temperature profile and the water abundance at depth. There are no current plans to measure the deep water abundance on the other giant planets. How the temperature profile changes with latitude will allow the atmospheric circulation and wind speeds to be constrained to much greater depths than was possible using the Galileo probe (22 bar). There is a visible-wavelength camera on the spacecraft, primarily for outreach and public engagement purposes, but it will also image Jupiter's poles and low latitudes. With a resolution of 15 km per pixel at closest approach, investigations of small-scale features should be possible.

Cassini's Grand Finale at Saturn includes 22 proximal orbits (polar orbits within the rings) with periapse altitudes of about 5000 km, which will allow measurements of the gravity field up to J12. Similarly to the gravity measurements planned by Juno at Jupiter, this should allow resolution of the question of whether the observed cloud-level jets are a thin atmospheric layer phenomenon or reflect deep cylindrical dynamics. These measurements by Cassini will also likely allow better constraints to be put on Saturn's rotation rate (Helled et al., 2015). In combination with the known gravity constraints for Uranus and Neptune (Kaspi et al., 2013), these gravity measurements by Juno and Cassini should enable us to finally narrow down the possible mechanisms driving zonal jets on giant planets within the next few years.

JUICE is to be launched in the early 2020s (Dougherty et al., 2011) and due to arrive in orbit around Jupiter in 2029, where it will primarily study Europa, Callisto and Ganymede, going into orbit around Ganymede in late 2032. JUICE will combine a large spectral range in its instrumentation with surveys of a wide range of space- and timescales afforded by the spacecraft's orbit and proposed planetary tour, in particular detailed coverage of Jupiter's poles during the high-inclination phase. It will be able to map the planet with global coverage at high resolution (~tens of kilometers) over a long period, important for understanding jet variability, eddy momentum fluxes, the relative importance of barotropic and baroclinic processes, and the roles of storms, waves and other nonglobal phenomena. Using the on-board Ultra Stable Oscillator, JUICE will be able to perform occultation measurements of Jupiter with unprecedented accuracy and global coverage. This will allow mapping of the atmospheric winds and composition down to a level of several bar. Using high-resolution submillimeter spectroscopy it will be possible to measure winds in the stratosphere via direct Doppler measurements.

While a Uranus mission has not yet been selected, there is considerable interest in such a venture. Such a mission would do the same for those planets as for Jupiter and Saturn, moving our understanding of these planets' interior and atmosphere, along with their satellites and rings, from exploration to characterization. This is particularly important due to the large numbers of Neptune-type exoplanets that have been discovered over the past several years, and for which Uranus and Neptune serve as prototypes.

As well as orbiters, a desired goal for future missions to the giant planets is to put a probe into Saturn's atmosphere, as was done with the Galileo probe for Jupiter. Like the Galileo probe, this would focus on the chemical composition of the planet and noble gas inventories, fundamental for understanding Solar System formation, but also for atmospheric dynamics (Mousis et al., 2014).

In terms of continuous monitoring of Jupiter's and Saturn's atmospheric dynamics, there is interest in a dedicated small space telescope to monitor the dynamics of these planets' atmospheres in the visible and near-infrared bands (Wong et al., 2009). In the absence of such a mission (or complementary to it), there are an increasing number of amateur observers who are able to produce regular observations resulting in a global monitoring of the giant planets' atmospheric activity (Hueso et al., 2010). Laboratory experiments and models of deep zonal flows, such as those recently presented by Cabanes et al. (2017), will allow better understanding and simulation of the giant and icy planets' zonal jets.

4.16.3 Modeling and Theory

Future work in numerical modeling is primarily focused on including processes relevant to the energy sources driving the zonal jets. In particular, these include small-scale convective and moist processes, and how these interact with the stratified atmosphere. With more sophisticated models it should be possible to determine whether baroclinic instability can be driven by condensation-related temperature differences just above the water condensation level, and whether this translates into the jets and eddy momentum fluxes we see at the visible cloud levels at higher altitude. More sophisticated cumulus cloud parameterizations will be required in such models with plausible triggering, heating, cooling, and moistening and drying profiles. Similarly, the role of moist convection has become an important topic of study (e.g., Zuchowski et al., 2009); in particular, whether it can provide the requisite energy to drive the jets by itself.

Conversely, the processes responsible for dissipation also remain poorly understood. How important is radiative heating and cooling in regulating the tropospheric jets in a model with realistic heating profiles? Magnetohydrodynamic drag is a dissipative process often included in models. Whether it puts an effective upper lid on the influence of deep convective turbulence such that "weather layer" models terminating at some modest depth capture the processes directly relevant to maintaining the jets remains unknown.

In deeper models, is there a plausible (i.e. in a compressible atmosphere with realistic forcing and dissipation) deep convective cylinder explanation for observed giant planet jets? If so, does it apply only to the equatorial jets on these planets or to higher-latitude jets as well?

Improvements in computing power should make longer integration times more plausible in the future. The realism of current giant planet models is plagued by very long timescales that are impractical to simulate on today's computers, as actual radiative and frictional timescales are much longer than are currently achievable. Substantially longer integration times would go some way towards helping, although the timescales required are several orders of magnitude longer than is currently possible, particularly at depth, so this will not be a completely satisfactory solution.

Unlike Earth modeling work, there is not necessarily an ever-increasing drive towards greater horizontal resolution, although some of the scales responsible for important processes such as moist convective events are not yet fully resolved in global models. The vertical extent of three-dimensional "weather layer" models has been quite limited, typically limited to pressures between a few bar and a few mbar. A point will be reached where coupling between deep interior models and "weather layer" models is required, or shallow models will attain a sufficiently deep domain such that the (artificial) distinction between deep and shallow models is no longer necessary. Juno's observations of Jupiter's interior structure and the depth of its weather layer will be important in determining which of these two paradigms should be followed in the future in modeling Jupiter's zonal jets in particular.